Article

Cell Reports

Methionine Restriction Extends Lifespan in Progeroid Mice and Alters Lipid and Bile Acid Metabolism

Graphical Abstract

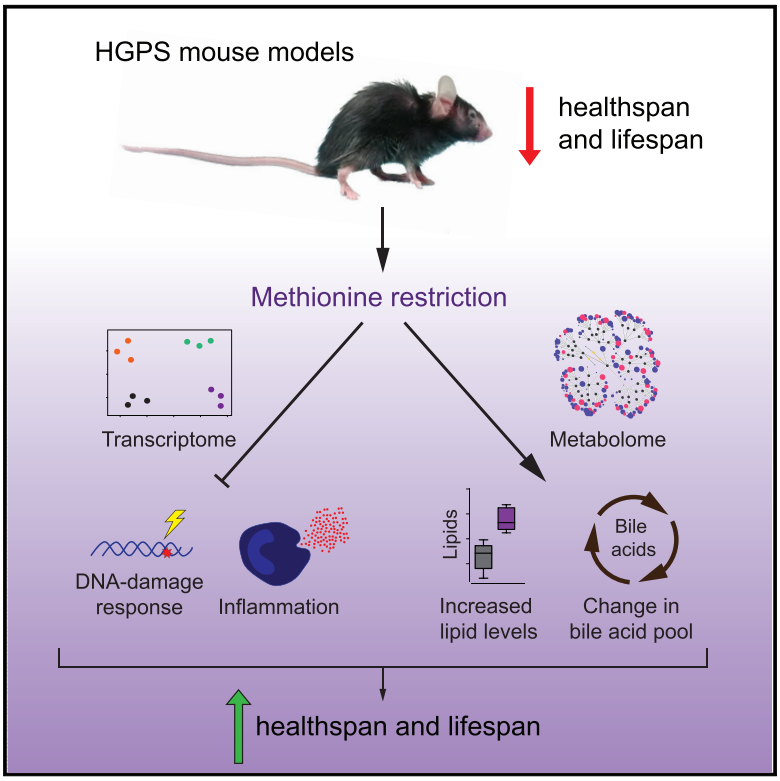

Authors

Clea Bárcena, Pedro M. Quirós, Sylvère Durand, ..., Guido Kroemer, José M.P. Freije, Carlos López-Otín

Correspondence

jmpf@uniovi.es (J.M.P.F.), clo@uniovi.es (C.L.-O.)

In Brief

Barcena et al. demonstrate that methionine restriction (MR) extends health span and lifespan in two mouse models of Hutchinson-Gilford progeria syndrome. MR attenuates transcriptional alterations in inflammation and DNA-damage response pathways and restores metabolomic dysregulation in the lipid and bile acid pool.

Highlights

- Methionine restriction (MR) extends health span and lifespan in progeroid mice
- MR reverts transcriptional alterations in inflammation and DNA-damage response pathways
- MR modifies the lipid and bile acid pool in *Lmna*^{G609G} mutant mice
- Diet enriched in cholic acid enhances health span and lifespan of progeria mice

Data and Software Availability

GSE117188

Bárcena et al., 2018, Cell Reports *24*, 2392–2403
August 28, 2018
https://doi.org/10.1016/j.celrep.2018.07.089

CellPress

OPEN ACCESS
CellPress

Cell Reports
Article

Methionine Restriction Extends Lifespan in Progeroid Mice and Alters Lipid and Bile Acid Metabolism

Clea Bárcena,[1,2] Pedro M. Quirós,[1,2] Sylvère Durand,[3,4,5,6] Pablo Mayoral,[1] Francisco Rodríguez,[1] Xurde M. Caravia,[1] Guillermo Mariño,[7,8] Cecilia Garabaya,[1] María Teresa Fernández-García,[9] Guido Kroemer,[3,4,5,6,10,11,12] José M.P. Freije,[1,2,*] and Carlos López-Otín[1,2,13,*]

[1]Departamento de Bioquímica y Biología Molecular, Facultad de Medicina, Instituto Universitario de Oncología (IUOPA), Universidad de Oviedo, 33006 Oviedo, Spain
[2]Centro de Investigación Biomédica en Red de Cáncer (CIBERONC), Madrid, Spain
[3]Cell Biology and Metabolomics Platforms, Gustave Roussy Cancer Campus, Villejuif, France
[4]Equipe 11 labellisée par la Ligue contre le Cancer, Centre de Recherche des Cordeliers, Paris, France
[5]INSERM, U1138, Paris, France
[6]Université Paris Descartes, Sorbonne Paris Cité, Paris, France
[7]Grupo Autofagia y Metabolismo, Instituto de Investigación Sanitaria del Principado de Asturias (IISPA), Oviedo, Spain
[8]Departamento de Biología Funcional, Facultad de Medicina, Universidad de Oviedo, 33006 Oviedo, Spain
[9]Unidad de Histopatología Molecular, IUOPA, Universidad de Oviedo, 33006 Oviedo, Spain
[10]Université Pierre et Marie Curie, Paris, France
[11]Pôle de Biologie, Hôpital Européen Georges Pompidou, AP-HP, Paris, France
[12]Karolinska Institute, Department of Women's and Children's Health, Karolinska University Hospital, Stockholm, Sweden
[13]Lead Contact
*Correspondence: jmpf@uniovi.es (J.M.P.F.), clo@uniovi.es (C.L.-O.)
https://doi.org/10.1016/j.celrep.2018.07.089

SUMMARY

Dietary intervention constitutes a feasible approach for modulating metabolism and improving the health span and lifespan. Methionine restriction (MR) delays the appearance of age-related diseases and increases longevity in normal mice. However, the effect of MR on premature aging remains to be elucidated. Here, we describe that MR extends lifespan in two different mouse models of Hutchinson-Gilford progeria syndrome (HGPS) by reversing the transcriptome alterations in inflammation and DNA-damage response genes present in this condition. Further, MR improves the lipid profile and changes bile acid levels and conjugation, both in wild-type and in progeroid mice. Notably, treatment with cholic acid improves the health span and lifespan *in vivo*. These results suggest the existence of a metabolic pathway involved in the longevity extension achieved by MR and support the possibility of dietary interventions for treating progeria.

INTRODUCTION

Over the past years, multiple studies have confirmed the idea that caloric restriction (CR), i.e., a reduction of caloric intake without malnutrition, can delay aging in numerous model organisms (Fontana and Partridge, 2015; Madeo et al., 2015). Thus, CR has been proven to act efficiently on several hallmarks of aging, enhancing metabolic flexibility, stem cell function, and DNA repair and reducing inflammation and age-related diseases (Finkel, 2015; López-Otín et al., 2013, 2016; Mitchell et al., 2016). Activation of AMPK, SIRT1, and the autophagy response and suppression of the growth hormone (GH)/IGF1 and mTOR signaling pathways have been implicated in the extension of the health span observed under CR (Breese et al., 1991; Burkewitz et al., 2014; Dunn et al., 1997; Fontana et al., 2016; Galluzzi et al., 2014; Johnson et al., 2013; Mercken et al., 2014; Stenesen et al., 2013). Recently, it has been described that CR extends the lifespan in a DNA-repair-deficient mouse model by reducing genomic stress (Vermeij et al., 2016). However, the underlying molecular pathways at the core of CR interventions remain incompletely defined. In this regard, the study of macronutrient restriction accomplished by the reduction of specific constituents of the diet instead of a simple and non-specific decrease in calorie intake has gained attention in recent years. Thus, restriction of proteins or certain amino acids in the diet can reduce the incidence of age-associated diseases and simultaneously increase lifespan (Mirzaei et al., 2014; Nakagawa et al., 2012; Solon-Biet et al., 2015). Among these, methionine restriction (MR) is supposed to exert its benefits, at least in part, through the suppression of the GH/IGF1 somatotrophic axis (Miller et al., 2005). MR also modulates mitochondrial activity, which, in turn, leads to an increase in both respiration rate (an increment of VO_2 and VCO_2) and energy expenditure (Orgeron et al., 2014) and increases the levels of hydrogen sulfide (H_2S), a molecule that is indispensable for lifespan extension under CR (Hine et al., 2015).

The effects of amino acid restriction have been assessed in normal aging yet remain unexplored in genetic models of accelerated aging. Hutchinson-Gilford progeria syndrome (HGPS) is a rare premature aging condition in which a point mutation in the

LMNA gene causes the accumulation at the nuclear envelope of an aberrant precursor of lamin A, named progerin (Eriksson et al., 2003; De Sandre-Giovannoli et al., 2003). Children with HGPS manifest growth impairment, lipodystrophy, and dermal and bone abnormalities, as well as cardiovascular alterations that lead to an average life expectancy of 13 years (Gordon et al., 2014). Of note, during normal human aging, ever-increasing amounts of progerin are produced as a result of *LMNA* aberrant alternative splicing, suggesting that progerin not only participates in the pathogenesis of HGPS but may also contribute to normal aging (Burtner and Kennedy, 2010; Scaffidi and Misteli, 2006). We have generated a mouse model carrying the equivalent of the most common human HGPS-associated mutation, p.Gly608Gly (p.Gly609Gly in mice). This model phenocopies most alterations observed in children with HGPS (Osorio et al., 2011). So far, the main manipulations that have led to an improvement of fitness and extension of lifespan in the p.Gly609Gly mouse model of HGPS have been a morpholino-based therapy that reduces progerin accumulation (Osorio et al., 2011), genetic or pharmacological attenuation of inflammation (Osorio et al., 2012), interruption of lamin A-progerin binding (Lee et al., 2016), inhibition of the acetyltransferase NAT10 (Balmus et al., 2018), and *in vivo* activation of reprogramming (Ocampo et al., 2016).

Here, we report that a low-methionine diet can extend health span and lifespan in the HGPS mouse model by ameliorating the alterations in signaling pathways,such as inflammation or DNA damage. Moreover, we describe that MR improves metabolic homeostasis and restores lipid and bile acid (BA) levels, and that treatment with cholic acid improves health span and lifespan in a mouse model of progeria. Together, our results suggest that the use of dietary interventions can effectively influence the metabolic deregulation of patients affected by accelerated aging syndromes, providing beneficial effects that could improve their quality of life and extend their longevity.

RESULTS

Methionine-Restricted Diet Extends Lifespan in a Mouse Model of HGPS

Mice homozygous for the HGPS mutation ($Lmna^{G609G/G609G}$ in a C57BL/6N background) were fed a diet with a low concentration (0.12%) of methionine. This dietary intervention reduced mortality rate and extended the median lifespan in both male and female $Lmna^{G609G/G609G}$ progeroid mice by 20% (Figures 1A, 1B, S1A, and S1B). Also, $Lmna^{G609G/G609G}$ mice fed an MR diet showed a tendency toward an increased maximum survival by approximately 20% (Figures 1A and S1C). As compared to wild-type (WT) controls, $Lmna^{G609G/G609G}$ mice on a control diet (CD) ($Lmna^{G609G/G609G}$-CD mice) are characterized by a relatively small size and low body weight (Osorio et al., 2011). Administration of the MR diet to $Lmna^{G609G/G609G}$ mice further exacerbated these characteristics (Figure 1C). Although $Lmna^{G609G/G609G}$-CD mice usually died by the time they reached a weight below 11 g, mice on the MR diet managed to survive with a lower weight for several weeks (Figure 1D), suggesting that small body size is not an obligatory predictor of health span in progeria. Indeed, MR retarded the appearance of lordokyphosis and loss of grooming in $Lmna^{G609G/G609G}$ mice (Figure 1E). $Lmna^{G609G/G609G}$ mice showed a basal loss of bone tissue due to inflammation-associated osteolysis, which is reversed under pharmacological and genetic inhibition of inflammation (Osorio et al., 2012). As expected, $Lmna^{G609G/G609G}$ mice with a CD showed a clear loss of bone tissue (Figures 1F and S1D). However, with an MR diet, we found an extensive amelioration of the phenotype with an almost complete recovery of bone structure. MR in $Lmna^{G609G/G609G}$ mice enhanced bone volume, number and connectivity of trabeculae, and bone mineral density in tibia, reaching values close to the normal ones found in WT animals (Figures 1F and S1D). Histological analysis showed that $Lmna^{G609G/G609G}$-CD mice had aortic alterations such as focal fibrosis with mild chronic infiltrate and an increment of matrix between elastic fibers. These alterations were not present in $Lmna^{G609G/G609G}$-MR mice (Figure 1G). Also, although both $Lmna^{G609G/G609G}$ mice on a CD and those on an MR diet had atrophy of the gastric mucosa, $Lmna^{G609G/G609G}$-CD mice presented glandular dilatations and ulcerations (Figure 1G). At the skeletal muscle, quadriceps, $Lmna^{G609G/G609G}$-CD mice had focal and perivascular fibrosis. Again, these alterations were absent in mice that were fed an MR diet (Figure 1G).

Analysis of Classical CR-Modulated Longevity Pathways in MR Progeria Mice

Similar to other mouse models of premature aging (Mariño et al., 2010; Niedernhofer et al., 2006; van der Pluijm et al., 2007), $Lmna^{G609G/G609G}$ mice display constitutive inhibition of the GH/IGF1 (insulin growth factor 1) pathway (Figure 2A), although an MR diet decreased glycemia under fasting conditions in both genotypes (Figure 2B). Reminiscent of published results on CR (Duffy et al., 1990; Heilbronn et al., 2006), MR caused a reduction in body temperature in WT mice. When compared to WT controls, however, $Lmna^{G609G/G609G}$ mice that were kept on a CD exhibited reduced body temperature (Figure 2C). Hence, a general reduction of metabolic turnover cannot explain the beneficial effect of MR on the progeroid phenotype. Also, although an MR diet enhanced AMPK and reduced mTORC1 activity in liver from WT mice (Figures 2D and S2), similarly to another model of HGPS (Mariño et al., 2008), $Lmna^{G609G/G609G}$-CD mice exhibited basal AMPK activation—demonstrated by its hyperphosphorylation—and an inhibition of mTORC1 in liver compared to WT mice, indicated by the reduced phosphorylation of its targets P70-S6K and AKT_{Ser473} (Figures 2D and S2). Of note, an MR diet induced a further decrease of AKT_{Ser473} phosphorylation in $Lmna^{G609G/G609G}$ mice, without changes in P70-S6K (Figures 2D and S2).

MR promotes an increase in respiration rates (VO_2 and VCO_2) and energy expenditure, features that were observed in WT mice fed an MR diet (Figures 2E–2G). On a CD, $Lmna^{G609G/G609G}$ mice exhibited a significant increment in respiration rates and energy expenditure when compared to WT animals (Figures 2E–2G), which could be explained as a possible strategy to increase thermogenesis. MR only slightly increased these values in $Lmna^{G609G/G609G}$ mice (Figures 2E–2G). On the basis of these results, we conclude that $Lmna^{G609G/G609G}$ mice have a basal activation of the pro-survival mechanisms of MR previously described, involving the GH/IGF1 axis, the AMPK/mTORC1

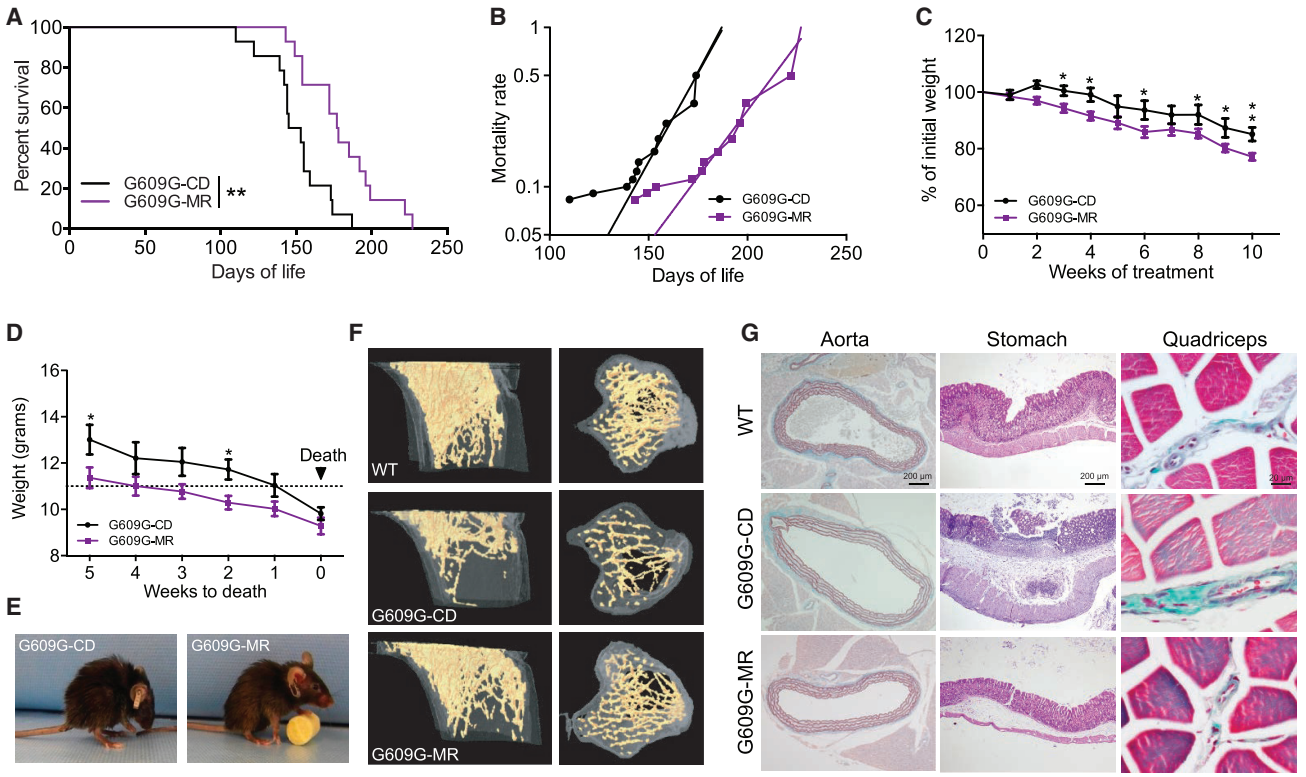

Figure 1. MR Enhances Lifespan and Health Span in *Lmna*$^{G609G/G609G}$ Mice

(A) Survival plot of *Lmna*$^{G609G/G609G}$ mice fed an MR diet (purple) or control diet (black) (n = 14 per group). Survival curves were analyzed with the log-rank (Mantel-Cox) test (p = 0.0023) and Gehan-Breslow-Wilcoxon test (p = 0.0044).

(B) Mice fed an MR diet show a lower mortality rate. Slope of G609G-CD is 0.022, and slope of G609G-MR is 0.016. Curve comparison: $p < 0.001$.

(C) MR diet in *Lmna*$^{G609G/G609G}$ mice induces a smaller weight. *$p < 0.05$ (CD, n = 11; MR, n = 12).

(D) Weight loss during the 5 weeks before death. *Lmna*$^{G609G/G609G}$-CD mice die by the time they reach a weight lower than 11 g, while *Lmna*$^{G609G/G609G}$-MR mice survive a lower weight. *$p < 0.05$ (n = 6 per group).

(E) *Lmna*$^{G609G/G609G}$-MR mice present a deceleration of the aged phenotype, appreciated by a retardation of lordokyphosis and a longer maintenance of grooming.

(F) Three-dimensional longitudinal and transversal images of tibias from WT-CD, *Lmna*$^{G609G/G609G}$-CD, and *Lmna*$^{G609G/G609G}$-MR littermate mice, generated with μCT analysis (n = 3 per group).

(G) Histological analysis of the aorta stained with orcein technique, gastric mucosa stained with H&E, and skeletal muscle (quadriceps) stained with H&E and Gomori trichrome.

Error bars indicate SEM. Scale bars are indicated in each figure. See also Figure S1.

energy sensors, thermoregulation, or general effects on energy expenditure. Therefore, the positive effects of MR on these progeroid mice cannot be explained exclusively by the classical CR pathways and should involve additional mechanisms.

MR Attenuates the Transcriptome Alterations of Progeroid Mice

To gain insight into the molecular mechanisms by which an MR diet extends lifespan in progeroid mice, we analyzed the transcriptome of liver tissues from fasted *Lmna*$^{G609G/G609G}$ and WT mice kept on a CD or MR diet. We selected this tissue because of its central metabolic function. Principal-component analysis indicated clear distinctions between the two genotypes and the two diets (Figure 3A). When compared to WT-CD, most transcripts altered in WT-MR mice were similarly changed in *Lmna*$^{G609G/G609G}$-MR mice. By contrast, there were more than 900 genes whose expression was altered in *Lmna*$^{G609G/G609G}$-CD but not in *Lmna*$^{G609G/G609G}$-MR mice, as compared to that from WT-CD mice (Figure 3B). Additionally, around 2,500 transcripts were changed in *Lmna*$^{G609G/G609G}$-MR mice and not in *Lmna*$^{G609G/G609G}$-CD when compared to WT-CD (Figure 3B), confirming a shift of the transcriptome landscape due to the dietary modification. Gene set enrichment analysis (GSEA) confirmed previously reported differences in transcript levels between *Lmna*$^{G609G/G609G}$ and WT mice, including those associated with the hyperactivation of inflammation and DNA-damage response pathways (Osorio et al., 2011, 2012), together with some undescribed downregulated pathways such as fatty acid metabolism and BA metabolism (Figure 3C). By comparing the transcript levels of *Lmna*$^{G609G/G609G}$-MR and *Lmna*$^{G609G/G609G}$-CD, we found that some of the pathways that were upregulated in progeroid models were repressed by MR in *Lmna*$^{G609G/G609G}$ mice. This applies to several groups of genes related to inflammation,

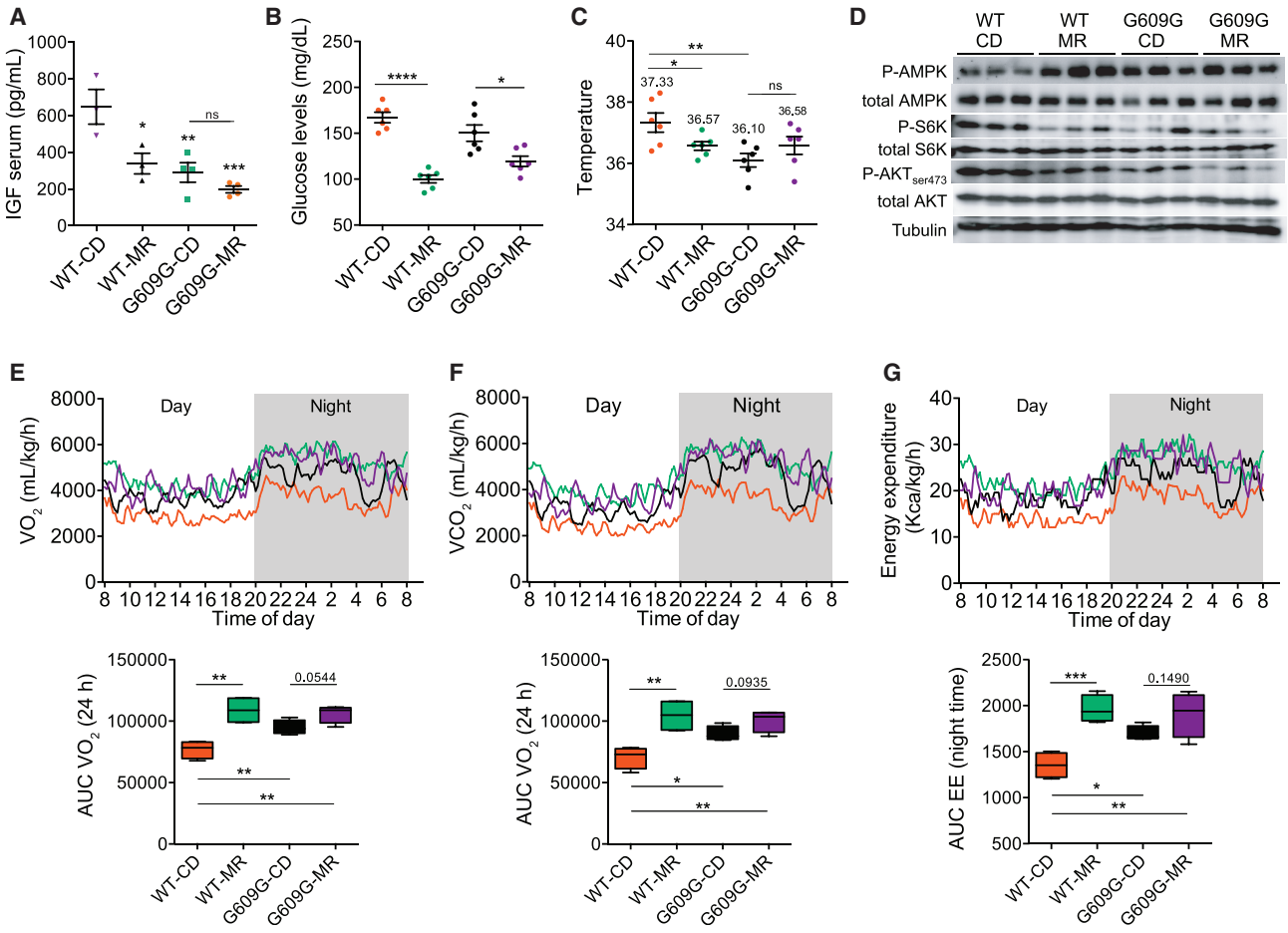

Figure 2. MR Fails to Induce the Classical Survival Response in *Lmna*$^{G609G/G609G}$ Mice

(A) Reduced basal levels of IGF1 in sera from *Lmna*$^{G609G/G609G}$ mice (WT, n = 3 per group; G609G = 4 per group).

(B) Glucose levels after a 5-hr fasting in the week 6 of treatment (n = 6 per group).

(C) Rectal temperature in week 6 of treatment (n = 6 per group).

For (A)–(C), lines in dot plots indicate mean ± SEM.

(D) Western blot analysis of phosphorylated (P)-AMPK, total AMPK, P-P70S6K, total P70S6K, P-AKT (ser473), and total AKT in liver protein extracts. The Western blots shown were carried out with the same samples run in parallel in three blots: one for P- and total (T)-AMPK, one for P- and T-P70S6K, and a third blot for P- and T-AKT and α-tubulin. All membranes were stained with Ponceau to confirm equal protein loading and homogeneous transfer.

(E–G). Indirect calorimetry. (E) VO_2 consumption (milliliters per kilogram per hour); (F) VCO_2 production (milliliters per kilogram per hour); and (G) energy expenditure (kilocalories per kilogram per hour) during 24 hr (n = 4 per group). Quantification of the area under the curve (AUC) of each parameter is provided below in boxplots (n = 4). *p < 0.05; **p < 0.01; ***p < 0.001.

See also Figure S2.

such as the interferon alpha and gamma response, tumor necrosis factor alpha (TNFA) signaling via nuclear factor κB (NF-κB), and interleukin-6 (IL-6), JAK, and STAT3 signaling. Also, DNA repair, BA metabolism, apoptosis, and p53 pathways were reduced by MR in *Lmna*$^{G609G/G609G}$ mice (Figure 3D).

Next, we compared the transcriptome profiles of *Lmna*$^{G609G/G609G}$ mice on either a CD or an MR diet with those of WT mice on a CD. Several pathways that are altered in the *Lmna*$^{G609G/G609G}$-CD mice with respect to WT controls were completely or partially rescued by MR (Figure 3E), as indicated by the fact that the GSEA-normalized enrichment score (NES) for *Lmna*$^{G609G/G609G}$-MR mice was opposite to the NES for *Lmna*$^{G609G/G609G}$-CD mice. This applies for IL-6, JAK, and STAT3 signaling, TNFA signaling via NF-κB, coagulation, complement, and KRAS signaling, indicating that MR was able to counteract progeria-associated changes in these pathways. For other pathways, such as fatty acid metabolism, apoptosis, E2F targets, and DNA repair, the NES values showed a partial improvement of the progeroid transcriptome upon MR (Figure 3E).

To identify possible genotype-specific responses, we performed GSEA of transcript levels from WT-MR versus WT-CD mice (Figure S3A). Most pathways were altered in the same direction as in *Lmna*$^{G609G/G609G}$-MR mice. Thus, mTORC1 signaling and xenobiotic, fatty acid and heme metabolism pathways were upregulated, whereas coagulation, complement, and

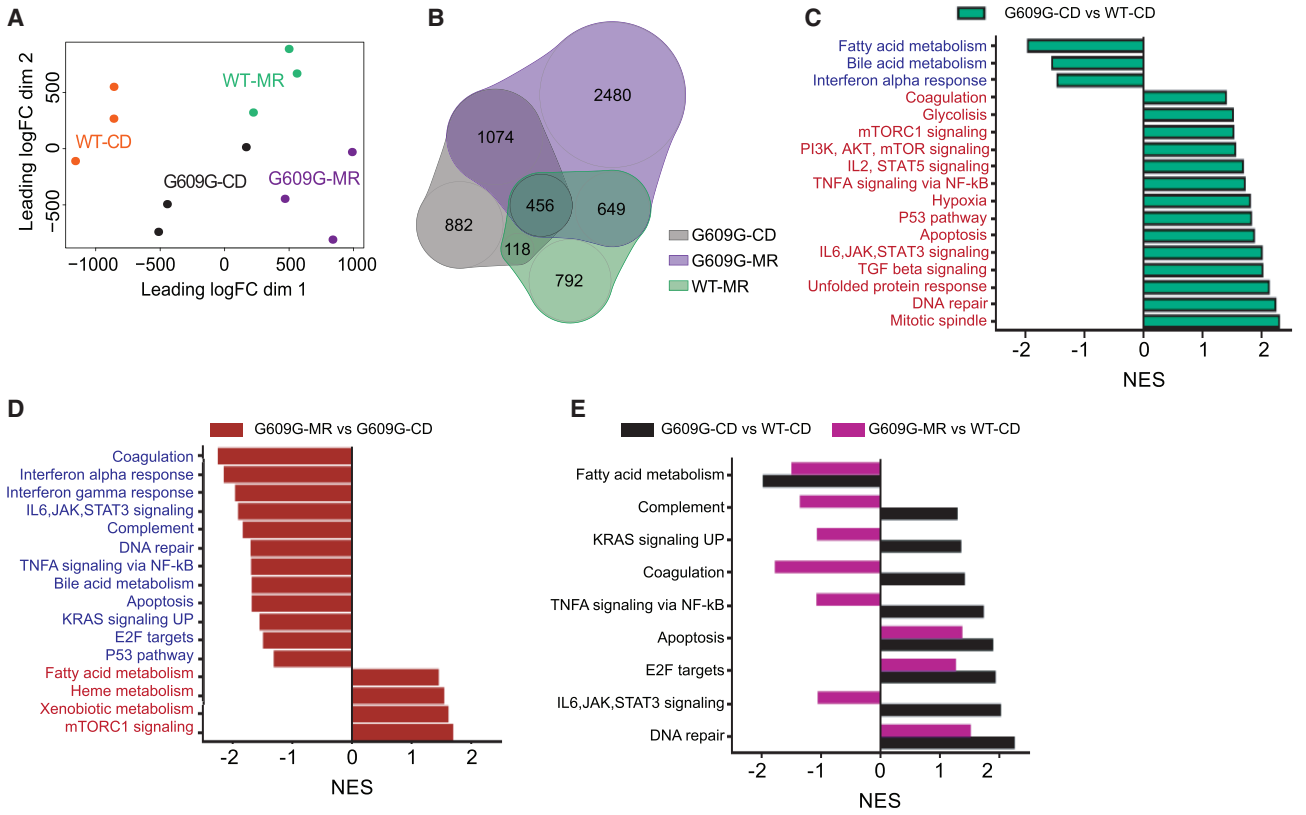

Figure 3. MR Restores the Transcriptome of *Lmna*$^{G609G/G609G}$ Mice

(A) Multidimensional scaling showed that the individual cases of our dataset were grouped according to the corresponding genotype and diet.

(B) Proportional Venn diagram illustrating that most of the transcripts modified by the MR diet were shared between *Lmna*$^{G609G/G609G}$ and WT mice.

(C and D) GSEA NES analysis of (C) *Lmna*$^{G609G/G609G}$ -CD versus WT-CD and (D) *Lmna*$^{G609G/G609G}$ -CD versus *Lmna*$^{G609G/G609G}$-MR mice. Red indicates upregulated pathways, and blue indicates downregulated pathways.

(E) GSEA NES comparison of *Lmna*$^{G609G/G609G}$-CD mice versus WT-CD mice and *Lmna*$^{G609G/G609G}$-MR mice versus WT-CD mice.

See also Figure S3.

interferon alpha and gamma response signaling were downregulated by MR. However, several other pathways were affected by MR in WT and *Lmna*$^{G609G/G609G}$ mice in opposite directions. This applied to pathways related to DNA damage (p53 pathway, DNA repair, and apoptosis) and inflammation (TNFA signaling via NF-kB and IL-6, JAK, STAT3 signaling), which were increased by MR in WT mice yet reduced in *Lmna*$^{G609G/G609G}$ mice. This difference might be related to the basal hyperactivation of these pathways in *Lmna*$^{G609G/G609G}$ mice on a CD (Figure 3C) (Osorio et al., 2011, 2012). Collectively, the aforementioned results indicate that MR attenuates or reverts several of the transcriptome alterations that accompany the phenotypic changes resulting from the *Lmna*$^{G609G/G609G}$ mutation, especially those accounting for inflammation and DNA-damage signaling.

MR Normalizes the Metabolome and Improves the Lipid Profile in the HGPS Mouse Model

To deepen the study of the changes induced by MR in both WT and progeroid mice, we performed mass spectrometric metabolome profiling in livers from fasted WT and *Lmna*$^{G609G/G609G}$ mice kept on a CD or an MR diet. This revealed clear genotype and diet effects, as determined by multidimensional scaling (Figure 4A) and unsupervised hierarchical clustering and heatmap analysis (Figure S4A). These results closely resemble those derived from the analysis of transcript levels, suggesting that the dietary intervention has more impact on metabolism than the *Lmna* mutation.

Examination of individual metabolites showed that MR depleted the methionine derivatives taurine, hypotaurine, and 5-methylthioadenosine. Thus, MR caused a 20-fold downregulation of taurine in WT and an 11-fold downregulation in *Lmna*$^{G609G/G609G}$ livers, together with an increment in glycine (Figures 4B, S4B, and S4C). MR also reduced quinolinic acid and phosphoserine (Figures 4B and S4B). Conversely, MR caused an increase in the polyamine spermidine by 10-fold in *Lmna*$^{G609G/G609G}$ livers (Figure 4B). Along with the increment in spermidine, MR caused an increase in some modified amino acids such as leucylproline and γ-glutamylleucine, intermediates of protein catabolism, as well as in dimethylglycine, which participates in choline and methionine metabolism (Figures 4B and S4B). MR also increased glycerophosphorylcholine, a choline derivative that plays a major role in osmotic balance (Figure 4B). In summary, an assessment of individual metabolites suggests that MR attenuates the difference between the metabolic

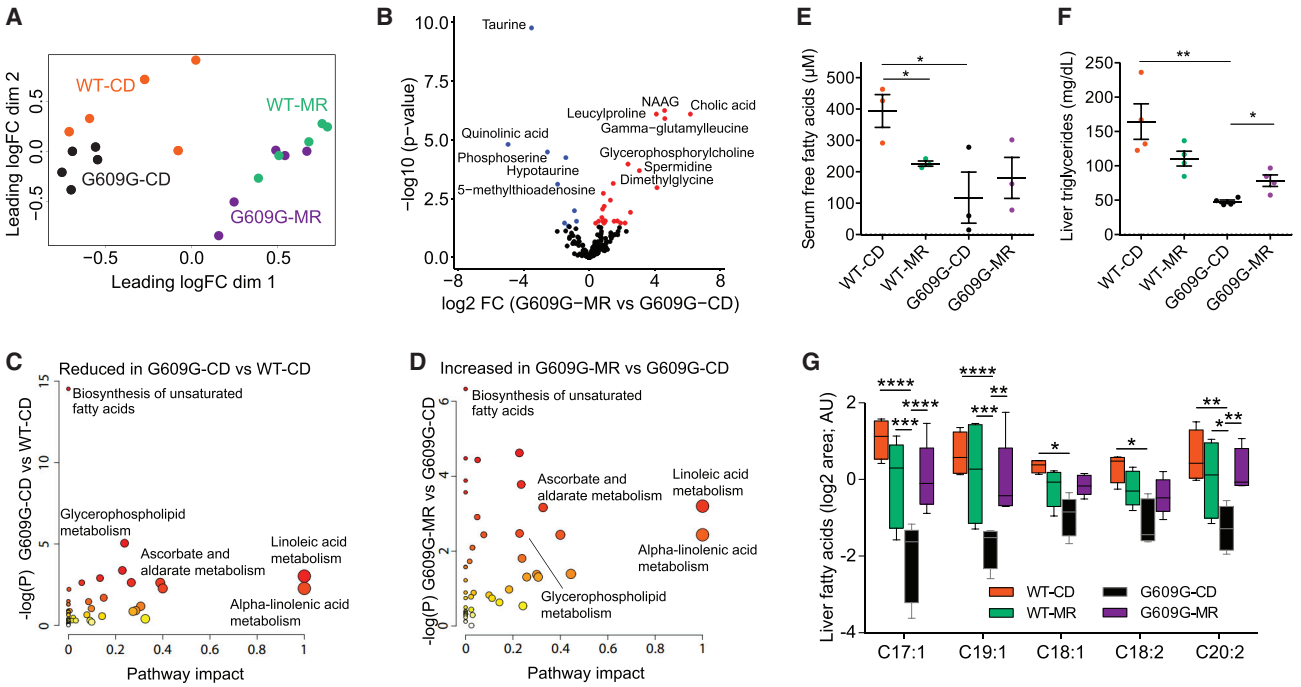

Figure 4. MR Restores Metabolome and Lipid Levels in *Lmna*$^{G609G/G609G}$ Mice

(A) Multidimensional scaling of the samples from the metabolomics analysis grouped according to the corresponding genotype and diet.

(B) Volcano plot showing the most differentially changed metabolites in *Lmna*$^{G609G/G609}$-MR compared to *Lmna*$^{G609G/G609G}$-CD mice. Upregulated metabolites are indicated in red, and downregulated metabolites are indicated in blue.

(C and D) Metabolic enrichment analysis showing (C) pathways downregulated in *Lmna*$^{G609G/G609G}$-CD compared to WT-CD mice and (D) pathways upregulated in *Lmna*$^{G609G/G609G}$-MR compared to *Lmna*$^{G609G/G609G}$-CD mice.

(E) Serum free fatty acid levels (in micromolar) (n = 3 per group).

(F) Liver triglyceride levels (n = 5 per group).

For (E) and (F), lines in dot plots indicate mean ± SEM.

(G) Relative liver levels of MUFAs (heptadecenoic (C17:1), nonadecenoic (C19:1) and oleic acid (C18:1)) and PUFAs (linoleic (C18:2) and eicosadienoic acid (C20:2)) in WT-CD, WT-MR, *Lmna*$^{G609G/G609G}$-CD, and *Lmna*$^{G609G/G609G}$-MR mice (WT, n = 4 per group; G609G, n = 5 per group). Levels represent the $\log_2$ of the normalized area in a.u. *p < 0.05; **p < 0.01; ***p < 0.001; ****p < 0.0001.

See also Figure S4 and Table S1.

landscapes from WT and *Lmna*$^{G609G/G609G}$ mice, inducing similar metabolic changes in both phenotypes.

Enrichment analyses using MetaboAnalyst led to the identification of pathways that were downregulated in *Lmna*$^{G609G/G609G}$ samples as compared to WT controls and that were reinstated by MR in the progeroid mice: biosynthesis of unsaturated fatty acids, glycerophospholipid metabolism, linoleic and alpha-linolenic acid metabolism, and ascorbate and aldarate metabolism (Figures 4C and 4D). Remarkably, in the aforementioned microarray analysis, we found that the expression of genes involved in fatty acid metabolism was reduced in *Lmna*$^{G609G/G609G}$-CD mice when compared to WT-CD mice and was partially recovered in *Lmna*$^{G609G/G609G}$-MR mice (Figures 3C and 3E). Among the molecules that were most reduced in *Lmna*$^{G609G/G609G}$-CD mice compared to WT-CD mice, we detected several fatty acids, such as palmitoleic, linoleic, oleic, and heptadecenoic acids (Figure S4D). Accordingly, we found that global serum free fatty acids and liver triglycerides were reduced in *Lmna*$^{G609G/G609G}$-CD mice and partly recovered on an MR diet (Figures 4E and 4F). MR also caused the recovery of several polyunsaturated (PUFAs) and monounsaturated fatty acids (MUFAs) in *Lmna*$^{G609G/G609G}$ mice, keeping their levels similar to those in WT-MR mice (Figure 4G). Altogether, we conclude that MR modifies the lipid profile in *Lmna*$^{G609G/G609G}$ mice and restores lipid metabolic pathways that were repressed in progeroid mice.

MR in Progeroid Mice Increases BA Levels in Liver under Fasting Conditions and Reverts the High Levels of Taurine Conjugation

In the microarray analysis described earlier, we also noted differences in BA metabolism at the transcriptional level in *Lmna*$^{G609G/G609G}$ mice under a CD when compared to both WT-CD and *Lmna*$^{G609G/G609G}$-MR mice (Figures 3C and 3D). The metabolomic profiling further allowed us to explore this alteration, which revealed that cholic acid was downregulated (11 times) in *Lmna*$^{G609G/G609G}$-CD mice versus WT-CD mice (Figure S4D) yet upregulated by 7 and 12 times in *Lmna*$^{G609G/G609G}$-MR and WT-MR mice, respectively (Figure 5A). Notably, cholic acid was upregulated 85-fold in *Lmna*$^{G609G/G609G}$-MR mice versus *Lmna*$^{G609G/G609G}$-CD mice, being the metabolite most induced by MR (Figures 4B and S4B). As shown earlier, taurine

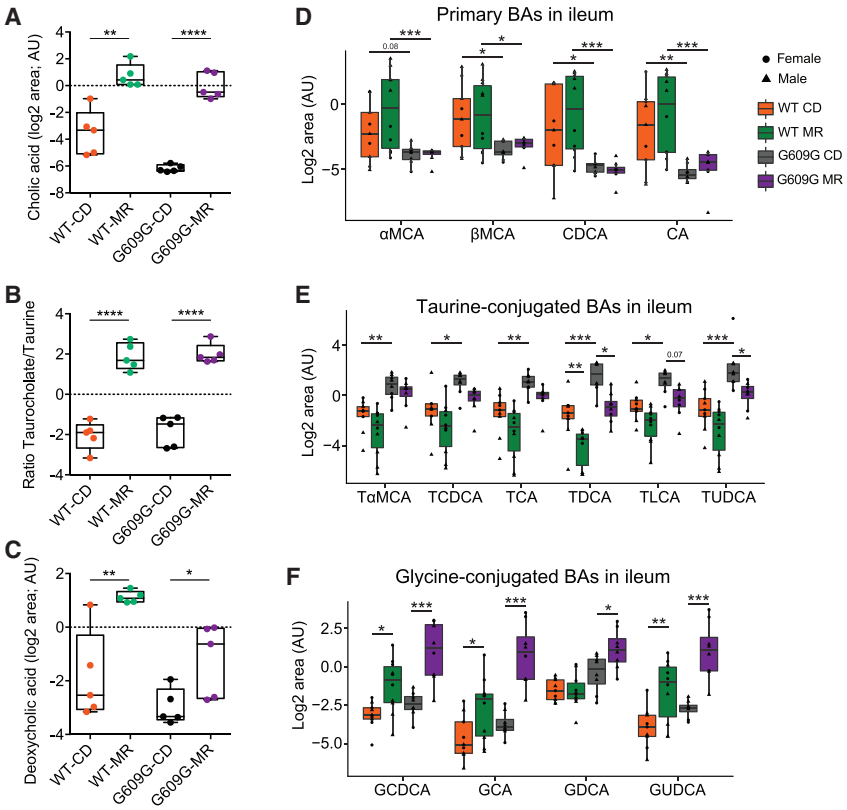

Figure 5. Profiling BA Levels in Fasting and Re-feeding Conditions Shows a Loss of Primary BAs in *Lmna*$^{G609G/G609G}$ Mice and an Abnormal Increment in Taurine Conjugation

(A–C) Boxplots showing the (A) levels of cholic acid, (B) taurocholate/taurine ratio, and (C) levels of deoxycholic acid under fasting conditions in liver samples from WT-CD, WT-MR, *Lmna*$^{G609G/G609G}$-CD and *Lmna*$^{G609G/G609G}$-MR (n = 5 per group). Levels of cholic and deoxycholic acid are presented as the log^2 of the normalized area in a.u. (AU).

(D–F) Boxplots showing the levels of (D) primary BAs, (E) taurine-conjugated BAs, and (F) glycine-conjugated BAs in ileum samples from WT-CD, WT-MR, *Lmna*$^{G609G/G609G}$-CD and *Lmna*$^{G609G/G609G}$-MR mice under refeeding conditions (n = 8 per group). Levels represent the log$_2$ of the normalized area in a.u. Sex is indicated with different symbols. αMCA, α-muricholic acid; βMCA, β-muricholic acid; CDCA, chenodeoxycholic acid; CA, cholic acid; TαMCA, tauro-α-muricholic acid; TCDCA, taurochenodeoxycholic acid; TCA, taurocholic acid; TDCA, taurodeoxycholic acid; TLCA, taurolithocholic acid; TUDCA, tauroursodeoxycholic acid; GCDCA, glycochenodeoxycholic acid; GCA, glycocholic acid; GDCA, glycodeoxycholic acid; GUDCA, glycoursodeoxycholic acid.

*p < 0.05; **p < 0.01; ***p < 0.001; ****p < 0.0001. See also Figure S5 and Table S2.

was severely downregulated in progeroid mice under MR (Figures 4B and S4C); however, BAs conjugated with taurine, such as taurocholic or taurodeoxycholic acid, were not changed upon MR in liver (Figures S5A and S5B). This implied that the ratio of taurocholic acid to taurine was remarkably upregulated in both *Lmna*$^{G609G/G609G}$ and WT mice maintained on MR (Figure 5B). The secondary BA deoxycholic acid was also decreased in *Lmna*$^{G609G/G609G}$-CD mice versus WT-CD mice and increased upon MR in both *Lmna*$^{G609G/G609G}$ and WT mice (Figure 5C), thus exhibiting a pattern of modulation similar to that of cholic acid.

To understand the alteration of BAs in *Lmna*$^{G609G/G609G}$ mice, we examined the mRNA expression levels of enzymes involved in their generation, including those encoding components of the cytochrome P450 complex (Lorbek et al., 2012). mRNA expression analysis of Cyp7a1, Cyp7b1, Cyp8b1, Cyp3a11, and Cyp39a1 in liver showed that the only enzyme consistently activated in both WT and progeroid mice fed an MR diet was Cyp39a1 (Figure S5C). Of note, Cyp39a1 is involved in alternative pathways of BA synthesis (Lorbek et al., 2012); in contrast, Cyp7b1 and Cyp8b1, key enzymes in the classical and alternative synthesis pathway of BAs, were repressed under an MR diet (Figure S5C). These results suggest that the increment in BAs observed under an MR diet does not depend on an increment of the synthesis pathways described so far.

To deepen the origin of the changes observed in BAs in WT and progeroid mice on a CD and an MR diet, we profiled BA levels in liver and ileum through targeted metabolomics under refeeding conditions, when BA synthesis is induced. We observed that, under this nutritional condition, levels of primary BAs in ileum were reduced in progeroid mice on both a CD and an MR diet (Figure 5D); however, this trend was not observed in liver (Figure S5D). These results suggest that the increment in primary BAs observed in liver in MR-fed mice under fasting conditions was not dependent on their synthesis. Indeed, no differences were observed in the transcript levels of key enzymes involved in the generation of BAs upon refeeding conditions (Figure S5E). Remarkably, and similar to fasting conditions, Cyp39a1 was the only enzyme induced by an MR diet in both genotypes (Figure S5E). *Lmna*$^{G609G/G609G}$-CD mice had abnormally high levels of BAs conjugated with taurine in ileum of both sexes (Figure 5E). On an MR diet, the levels of taurine-conjugated BAs were lower (Figure 5E), probably due to the taurine deficiency associated with the modified diet (Figure S4C). Conversely, both WT and *Lmna*$^{G609G/G609G}$ mice fed the MR diet showed an increment in glycine-conjugated BAs, such as glycochenodeoxycholic acid (GCDCA), glycocholic acid (GCA), glycodeoxycholic acid (GDCA), and glycoursodeoxycholic acid (GUDCA) (Figure 5F). Glycine-conjugated BAs, which are usually found in much lower levels than taurine-conjugated BAs, are not synthetized in mouse liver but generated by the gut microbiome in the ileum. Collectively, these results prove an alteration in the conjugation of BAs, with an excess of taurine conjugation in *Lmna*$^{G609G/G609G}$-CD mice that is reversed in an MR diet, favoring this diet as an increment in glycine-conjugated BAs.

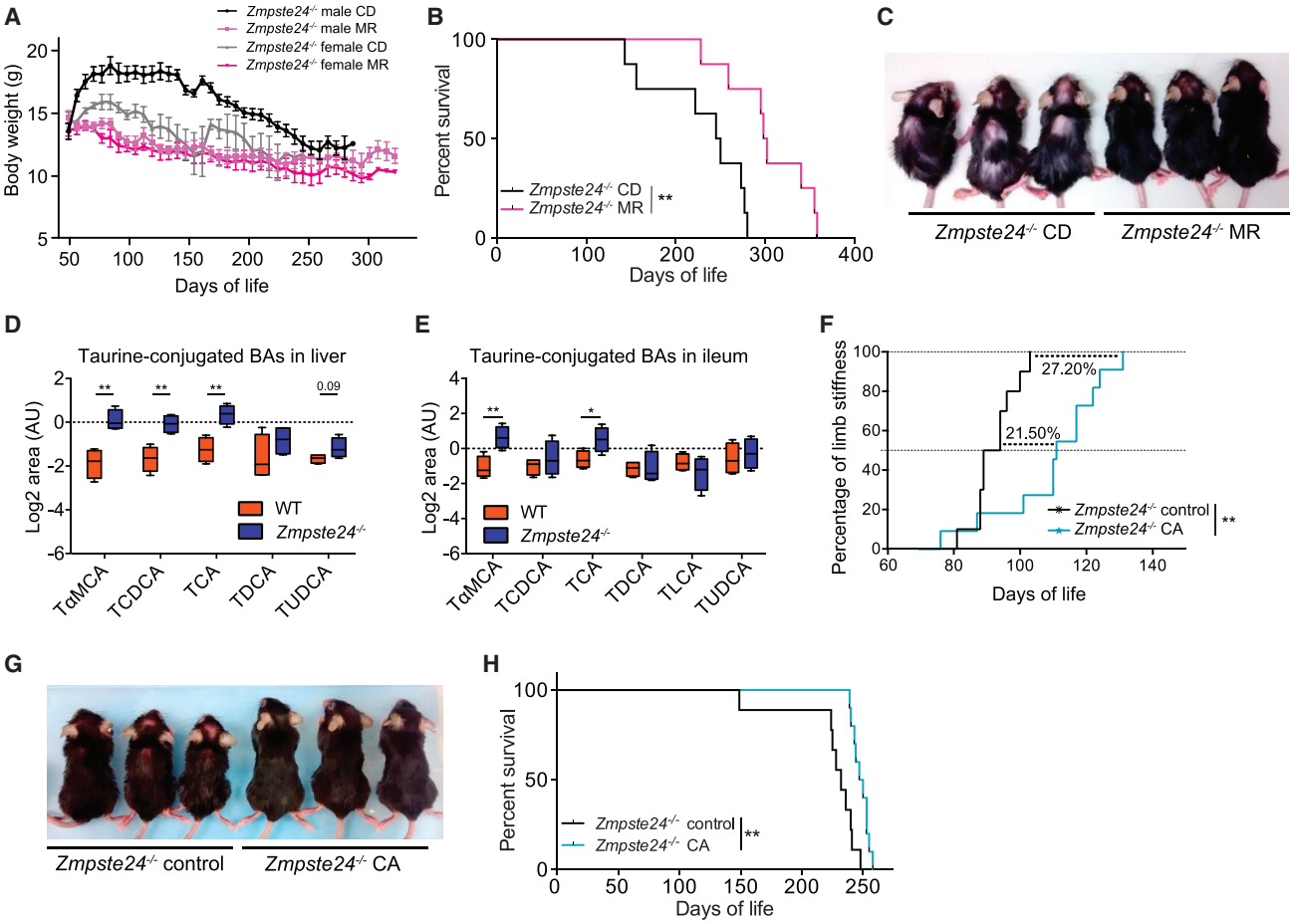

Figure 6. Both MR and *In Vivo* Modulation of BA Pool Exerts Beneficial Effects in *Zmpste24*$^{-/-}$ Mouse Model of Progeria

(A) *Zmpste24*$^{-/-}$ mice fed an MR diet (light and dark pink) show a lower weight than *Zmpste24*$^{-/-}$ mice under a CD (black and gray) (n = 4 per group).

(B) Survival plot of *Zmpste24*$^{-/-}$ mice fed an MR diet (pink) or CD (black) (n = 8 per group). Survival curves were analyzed with the log-rank (Mantel-Cox) test (p = 0.0029) and Gehan-Breslow-Wilcoxon test (p = 0.008).

(C) *Zmpste24*$^{-/-}$ MR mice show a healthier aspect, manifested by a reduced loss of hair and improved cervicothoracic lordokyphosis, than *Zmpste24*$^{-/-}$ CD mice.

(D and E) Taurine-conjugated BAs in (D) liver and (E) ileum samples from WT and *Zmpste24*$^{-/-}$ female mice (n = 4 per group). Levels represent the $\log_2$ of the normalized area in a.u. TαMCA, tauro-α-muricholic acid; TCDCA, taurochenodeoxycholic acid; TCA, taurocholic acid; TDCA, taurodeoxycholic acid; TLCA, taurolithocholic acid; TUDCA, tauroursodeoxycholic acid.

(F) *Zmpste24*$^{-/-}$ mice fed a diet enriched in cholic acid (*Zmpste24*$^{-/-}$ CA) show a retarded manifestation of the phenotype-associated hindlimb stiffness compared to *Zmpste24*$^{-/-}$ mice fed the CD (*Zmpste24*$^{-/-}$ control). Appearance of limb stiffness was analyzed with the log-rank (Mantel-Cox) test (p = 0.001) and Gehan-Breslow-Wilcoxon test (p = 0.0089) (n = 10 per group).

(G) *Zmpste24*$^{-/-}$ CA mice (right) show a healthier aspect, manifested by a bigger size, reduced loss of hair, and improved cervicothoracic lordokyphosis, compared to *Zmpste24*$^{-/-}$ control mice (left).

(H) Survival plot of *Zmpste24*$^{-/-}$ CA mice (n = 10) and *Zmpste24*$^{-/-}$ control mice (n = 10). Survival curves were analyzed with the log-rank (Mantel-Cox) test (p = 0.0011) and Gehan-Breslow-Wilcoxon test (p = 0.0012).

*p < 0.05; **p < 0.01. See also Figure S6 and Video S1.

MR Diet and *In Vivo* BA Supplementation Extends Health Span and Lifespan in *Zmpste24* Null Progeroid Mice

We explored whether the effects of MR observed in our *Lmna*$^{G609G/G609G}$ progeroid model could be reproduced in a different mouse model of premature aging and whether the alterations in BAs were also shared by different progeroid mice. Thus, we first evaluated the effect of MR in the *Zmpste24*$^{-/-}$ mouse model, deficient in the protease ZMPSTE24, which processes prelamin A into mature lamin A (Navarro et al., 2005; Pendás et al., 2002). As observed in *Lmna*$^{G609G/G609G}$ mice, *Zmpste24*$^{-/-}$ under MR (*Zmpste24*$^{-/-}$ MR) also showed improvements in health and survival. Despite their reduced size (Figure 6A), *Zmpste24*$^{-/-}$ MR mice had a 21% increase in median survival and an almost 28% increase in maximal survival (Figures 6B and S6A) and showed a healthier aspect, mostly apparent by a reduced loss of hair and improved atrophy of hindlimbs (Figures 6C and S6B).

Targeted metabolomics showed no differences in the levels of primary BAs in liver and ileum of *Zmpste24*$^{-/-}$ mice under re-feeding conditions in a CD (Figures S6C and S6D);

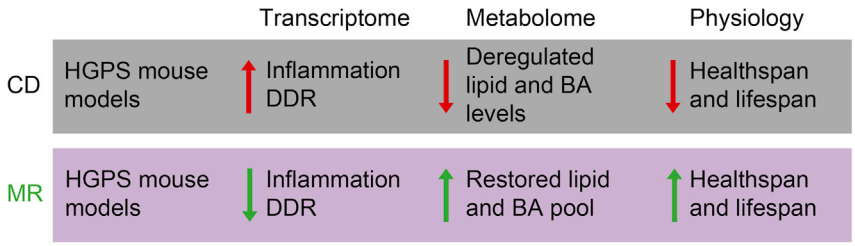

Figure 7. Effect of MR in Progeroid Mice
Mouse models of HGPS, such as *Lmna*$^{G609G/G609G}$ and *Zmpste24*$^{-/-}$, show increased systemic inflammation and hyperactivation of the DNA damage response (DDR) pathways when mice are maintained on a CD. The *Lmna*$^{G609G/G609G}$ mouse model also shows a deregulation of both lipid and BA levels. MR decreases the transcriptional activation of those stress pathways, restores lipid levels, and changes BA levels and conjugation. The attenuation of both transcriptional and metabolic alterations by MR increases health span and lifespan in both progeroid mouse models.

however, and similarly to *Lmna*$^{G609G/G609G}$ mice, these progeroid mice showed a significant increment in taurine conjugation (Figures 6D and 6E). These results indicate that progeroid mice have a common increment of taurine-conjugated BAs. MR shifted BA conjugation from an increase in taurine- to glycine-conjugated BAs (Figures 5E and 5F), which is independent of changes in primary BA synthesis after refeeding, opposite to the increase in primary BAs observed in fasting conditions. Based on these results, we hypothesize that BA supplementation could normalize BA levels and improve their health span. Therefore, we treated our *Zmpste24*$^{-/-}$ progeroid model, where health span is easier to assess than in *Lmna*$^{G609G/G609G}$ due to their longer survival, with the main primary BA, cholic acid. *Zmpste24*$^{-/-}$ mice kept on a diet enriched with 0.1% cholic acid (*Zmpste24*$^{-/-}$ CA) had a delayed appearance of the phenotype-associated hindlimb stiffness and a consequent improvement in their daily movement when compared to *Zmpste24*$^{-/-}$ mice fed a normal diet (*Zmpste24*$^{-/-}$ control) (Figures 6F and S6E; Video S1). Also, *Zmpste24*$^{-/-}$ CA had a milder loss of weight during the progression of the phenotype (Figure S6F). The healthier status of CA-treated progeroid mice was also assessed by their improved cervicothoracic lordokyphosis, reduced loss of hair, and bigger size (Figure 6G), as well as by their enhanced median survival (7%; Figure 6H) and tendency to an enhanced maximal survival (Figure S6G).

Collectively, these results indicate that MR promotes a healthier phenotype and extends survival in two different mouse models of progeria. Additionally, we have proved that *in vivo* supplementation of cholic acid in the diet exerts beneficial effects in progeria, suggesting that modulation of BA metabolism could have a key role regulating longevity in mice.

DISCUSSION

CR is the most effective intervention to prolong lifespan in diverse organisms so far; however, its application in humans presents important barriers, as food deprivation is something that not many people would accept to practice. This has led to the development of CR mimetics (Madeo et al., 2014; Mercken et al., 2012), although their use has limitations owing to the diverse effects of CR throughout different tissues (Igarashi and Guarente, 2016). In contrast, MR appears to be a simpler way of effectively acting on metabolism; more importantly, it offers a translational strategy that is easier to apply to humans (Mann et al., 1999; McCarty et al., 2009; Schmidt et al., 2016). The simplicity of a modified diet and the lack of negative secondary effects make this type of intervention a promising tool for future treatments of human diseases.

In the present work, we demonstrate that an MR diet can substantially rescue the pathologic phenotype observed in both the *Lmna*$^{G609G/G609G}$ and the *Zmpste24*$^{-/-}$ HGPS mouse models. With an MR diet, we found an amelioration of the most severely modified pathways, such as DNA repair and inflammation, and the normalization of certain metabolic alterations (Figure 7). Among the last, we detected a recovery in metabolic pathways related to lipid metabolism, supporting the role of lipid homeostasis in longevity (Schroeder and Brunet, 2015). Also, we observed that *Lmna*$^{G609G/G609G}$ mice have reduced levels of primary and secondary BAs in liver and that MR induces an increment of them in both WT and progeroid mice. Additionally, we found that both *Lmna*$^{G609G/G609G}$ and *Zmpste24*$^{-/-}$ progeroid mice have abnormally high levels of taurine-conjugated BAs. Probably due to the deficiency in taurine under MR (Elshorbagy et al., 2010), mice fed with this diet have reduced taurine conjugation with increased glycine conjugation. As a result, the excess of taurine-conjugated BAs observed in progeroid mice is reverted. We also showed that the addition of 0.1% cholic acid in the diet has a beneficial outcome in both the health span and lifespan of an HGPS mouse model. Previous studies have suggested a role of BAs in the promotion of health and longevity in different organisms, from lower eukaryotes to mammals. BAs—and, in particular, lithocholic acid—extend longevity in yeast in an mTOR-independent manner (Arlia-Ciommo et al., 2014; Goldberg et al., 2010; Leonov et al., 2017). Also, loss of the bile-acid-like steroids called dafachronic acids reduces fitness and lifespan in *C. elegans* (Magner et al., 2013). Conversely, in the long-lived *Ghrhr*$^{-/-}$ mice, there is an increase in BA levels in bile, serum, and liver (Amador-Noguez et al., 2007). In our study, we observed that MR can substantially rescue the phenotype of the HGPS mouse, and we suggest that this occurs, at least in part, by modulating the BA profile. However, the exact mechanism by which MR affects BAs levels and improves health span and lifespan remains to be elucidated.

Overall, we provide evidence that diet modulation can effectively increase health and the lifespan, not only in a normal physiological situation but also in two mouse models of accelerated aging, hence opening the possibility for implementing diet-based strategies for the treatment of these diseases.

EXPERIMENTAL PROCEDURES

Additional details and resources used in this work can be found in the Supplemental Experimental Procedures.

Mouse Models

Lmna$^{G609G/G609G}$ and *Zmpste24*$^{-/-}$ mice in a C57BL/6N background were generated by crossing heterozygous mice and genotyped in our laboratory as previously described (Osorio et al., 2011; Varela et al., 2005). Mice were bred in a specific pathogen-free (SPF) area, and the experiments were carried out in a conventional area with exclusion barriers. Mice were caged separately by sex and genotype and were checked daily for water and food supplies, as well as for good physical condition. Experiments with modified diets were initiated at 7 weeks of age. For the microarray analysis and untargeted metabolomics under fasting conditions, 6 males per group were sacrificed after 6 hr of fasting at 110 days of life and used to obtain serum and tissue samples. For the BA profiling under refeeding conditions, mice were fasted overnight and then allowed to feed *ad libitum* for 4 hr before being sacrificed. All animal experiments were approved by the Committee for Animal Experimentation of the Universidad de Oviedo and were performed in accordance with its guidelines, making every effort to minimize the suffering of the mice.

Diet Treatment

Rodent diets used in this study were acquired from Research Diets. The control diet (A11051302) contains a 0.86% of methionine, whereas the methionine-restricted diet (A11051301) contains 0.12% methionine. Cystine was not added to the diets during their elaboration. Methionine-restricted and control diets were provided that combined solid and crushed pellets in all experimental groups to facilitate the feeding of the mutant mice. A diet enriched in cholic acid was prepared with a dried ground global diet (Envigo #2014S); it was mixed with filtered water (0.8 mL/g) containing, in suspension, cholic acid (Sigma, #C1129) to obtain a final concentration of 0.1% in the resulting diet. The mixture was kneaded to form pellets that were allowed to dry overnight in a hood, resulting in small pellets of soft consistency.

Histological Analysis

Tissues were fixed in 4% paraformaldehyde in PBS and stored in 70% ethanol. Fixed tissues were embedded in paraffin by standard procedures. Blocks were sectioned (5 μm) and stained with H&E (stomach), orcein (aorta), or H&E with Gomori trichrome (muscle).

Analysis of Bone Structure

All tibia samples were scanned by high-resolution micro-computed tomography (SkyScan 1174, SkyScan, Kontich, Belgium). The parameters were measured according to the American Society for Bone and Mineral Research (ASBMR) histomorphometry nomenclature (Parfitt et al., 1987).

Metabolic and Movement Measurements

Metabolic parameters such as VO_2, VCO_2 and energy expenditure, as well as daily movement, were obtained using the CLAMS Comprehensive Lab Animal Monitoring System (Oxymax CLAMS, Columbus Instruments) and analyzed following the manufacturer's instructions. Mice were monitored for 48 hr, and the first 24 hr were discarded in the analysis, as this was considered an acclimation period.

Western Blot Analysis

Tissues were collected and immediately frozen in dry ice. Samples were processed for western blotting using standard methods. Antibodies against phospho-P70S6K (Thr421/Ser424) (#9204), total P70S6K (#2708), phospho-AKT (Ser473) (#9271), total AKT (#9272), phospho-AMPKα (#2531), and total AMPKα (#2532) were obtained from Cell Signaling Technology, and α-Tubulin (T6074) was obtained from Sigma.

IGF1 Analysis, Serum Fatty Acids, and Liver Triglycerides

IGF1 measurements were performed in serum with EDTA using an IGF1 ELISA kit obtained from R&D Systems (MG100). Free fatty acids in serum were assayed using the luminometric Free Fatty Acid Assay Kit from Abnova (KA1667). Triglycerides in liver were assayed using the EnzyChrom Triglyceride Assay Kit from BioAssay Systems (ETGA-200).

Microarray Profiling

Microarray profiling was performed as previously described (Osorio et al., 2011), using a GeneChip Mouse Gene 1.0 ST Array (Affymetrix). Raw data were processed with the RMAExpress program (http://RMAExpress.bmbolstad.com), using default settings. Differentially expressed genes in each condition were identified using the R/Bioconductor package limma (Ritchie et al., 2015). A proportional Venn diagram was generated using nVenn (http://degradome.uniovi.es/cgi-bin/nVenn/nvenn.cgi) (Pérez-Silva et al., 2018). GSEA v2.2.0 and MSigDB release 5.1 (http://software.broadinstitute.org/gsea/index.jsp) were used for pathway enrichment analysis. Weighted enrichment scores were calculated with gene expression lists ranked by signal-to-noise ratio (maximum gene set size: 500; minimum gene set size: 20; number of permutations: 1,000; gene set database: Hallmark; false discovery rate [FDR] $\leqslant$ 0.25; and p $\leqslant$ 0.01). Plots representing GSEA NESs were generated using GraphPad Prism 6.0.

Untargeted and Targeted Metabolomics Analysis

Metabolites were extracted from 30 mg of each tissue using a mix of cold methanol/water/chloroform (9:1:1). Samples were homogenized, and phase separation was performed by centrifugation. For untargeted metabolomics, supernatants were collected and evaporated, and dried extracts were solubilized in methanol. Two aliquots were produced for gas chromatography-mass spectrometry (GC-MS) and liquid chromatography-mass spectrometry (LC-MS) analysis. For targeted metabolomics, collected supernatants were evaporated, dried, and solubilized with MilliQ water. One aliquot was transferred to LC vials and injected into LC-MS. Targeted metabolomics were performed using ultra-high-pressure liquid chromatography coupled to mass spectrometry (UHPLC-MS). Analytical methods and data processing were performed as previously described (Enot et al., 2015). Results were represented as the normalized area of the MS picks in $\log_2$ scale using a.u. Normalization was performed by correcting the area of the MS picks across the batches using the quality control (QC) pooled samples (regularly injected during the analysis) and by centering their values around the mean of the QC areas. Differentially expressed metabolites were identified using the R/Bioconductor package limma (Ritchie et al., 2015). Metabolic pathway analysis was performed with MetaboAnalyst 3.0 (http://www.metaboanalyst.ca/) (Xia et al., 2015), using the hypergeometric test for representation analysis, and relative-betweenness centrality was selected for pathway topology analysis. For targeted metabolomics, statistical differences in BAs were calculated using a one-way ANOVA with Tukey's multiple comparison post hoc test, including sex as cofactor.

Statistical Analysis

Unless otherwise specified, all experimental data are reported as mean ± SEM, except for the boxplots that were generated using Tukey's method. Statistical differences were calculated using two-tailed Student's t test for pairwise comparisons between two groups and one-way ANOVA with Tukey's correction for multiple comparisons for more than two groups. Survival analysis was performed by using the Kaplan-Meier method, and statistical differences were analyzed with the log-rank (Mantel-Cox) test and Gehan-Breslow-Wilcoxon test. Power analysis of survival was 80%. Mortality rate was calculated using the Gompertz model. Statistical differences between mortality curves was calculated using the extra-sum-of-squares F test. Maximal survival was analyzed using one-tailed Fisher's exact test at the 80th percentile (Wang et al., 2004). All statistical tests, data analysis, and plots were generated using R and RStudio (R Core Team, Vienna, Austria, https://www.r-project.org; RStudio Team, Boston, MA, USA, https://www.rstudio.com) and GraphPad Prism 6.0. Plots and figures were modified using Adobe Illustrator CC.

DATA AND SOFTWARE AVAILABILITY

The accession number for the microarray data and raw files reported in this paper is GEO: GSE117188.

SUPPLEMENTAL INFORMATION

Supplemental Information includes Supplemental Experimental Procedures, six figures, three tables, and one video and can be found with this article online at https://doi.org/10.1016/j.celrep.2018.07.089.

ACKNOWLEDGMENTS

We thank Drs. V. Quesada, A. Fueyo, A.R. Folgueras, G. Velasco, M. Mittelbrunn, and J. M. Fraile for helpful comments and advice; and R. Feijoo, A. Moyano, and S. Alvarez-Miranda for excellent technical assistance. We also thank M.S. Pitiot, V. García de la Fuente, M.C. Muñiz, V. Loredo, and E. Pascual for histological and micro-computed tomography (μCT) analysis. We also acknowledge the generous support by J.I. Cabrera. The Instituto Universitario de Oncología is supported by the Fundación Bancaria Caja de Ahorros de Asturias. C.L.-O. is supported by grants from the European Union (ERC-2016-ADG, DeAge); Ministerio de Economía y Competitividad (MINECO/FEDER: SAF2014-52413-R and SAF2017-87655-R); Instituto de Salud Carlos III (RTICC); Progeria Research Foundation (PRF2016-66); and EDP Foundation. J.M.P.F. is supported by the Ministerio de Economía y Competitividad (MINECO/FEDER: SAF2015-64157-R) and Gobierno del Principado de Asturias. G.M. is funded by the Ramón y Cajal Program (RYC-2013-12751) and supported by the Ministerio de Economía y Competitividad (MINECO/FEDER: BFU2015-68539) and BBVA Foundation (BBM_BIO_3105). G.K. is supported by the Ligue contre le Cancer (équipe labelisée); Agence National de la Recherche (ANR) – Projets Blancs; ANR under the frame of E-Rare-2; the ERA-Net for Research on Rare Diseases; Association pour la Recherche sur le Cancer (ARC); Cancéropôle Ile-de-France; Institut National du Cancer (INCa); Institut Universitaire de France; Fondation pour la Recherche Médicale (FRM); the European Commission (ArtForce); the European Research Council (ERC); the LeDucq Foundation; the LabEx Immuno-Oncology; the SIRIC Stratified Oncology Cell DNA Repair and Tumor Immune Elimination (SOCRATE); the SIRIC Cancer Research and Personalized Medicine (CARPEM); and the Paris Alliance of Cancer Research Institutes (PACRI).

AUTHOR CONTRIBUTIONS

C.B., P.M.Q., C.L.-O., and J.M.P.F. conceived and designed experiments. C.B., P.M.Q., P.M., F.R., X.M.C., G.M., and C.G. performed experiments and analyzed data. S.D. and G.K. performed metabolomics. M.T.F.-G. performed histopathological analysis. C.B., C.L.-O., and J.M.P.F. wrote the manuscript, and P.M.Q. and G.K. contributed to the editing and proofreading.

DECLARATION OF INTERESTS

The authors declare no competing interests.

Received: October 13, 2016
Revised: March 10, 2018
Accepted: July 27, 2018
Published: August 28, 2018

REFERENCES

Amador-Noguez, D., Dean, A., Huang, W., Setchell, K., Moore, D., and Darlington, G. (2007). Alterations in xenobiotic metabolism in the long-lived Little mice. Aging Cell *6*, 453–470.

Arlia-Ciommo, A., Piano, A., Leonov, A., Svistkova, V., and Titorenko, V.I. (2014). Quasi-programmed aging of budding yeast: a trade-off between programmed processes of cell proliferation, differentiation, stress response, survival and death defines yeast lifespan. Cell Cycle *13*, 3336–3349.

Balmus, G., Larrieu, D., Barros, A.C., Collins, C., Abrudan, M., Demir, M., Geisler, N.J., Lelliott, C.J., White, J.K., Karp, N.A., et al.; Sanger Mouse Genetics Project (2018). Targeting of NAT10 enhances healthspan in a mouse model of human accelerated aging syndrome. Nat. Commun. *9*, 1700.

Breese, C.R., Ingram, R.L., and Sonntag, W.E. (1991). Influence of age and long-term dietary restriction on plasma insulin-like growth factor-1 (IGF-1), IGF-1 gene expression, and IGF-1 binding proteins. J. Gerontol. *46*, B180–B187.

Burkewitz, K., Zhang, Y., and Mair, W.B. (2014). AMPK at the nexus of energetics and aging. Cell Metab. *20*, 10–25.

Burtner, C.R., and Kennedy, B.K. (2010). Progeria syndromes and ageing: what is the connection? Nat. Rev. Mol. Cell Biol. *11*, 567–578.

De Sandre-Giovannoli, A., Bernard, R., Cau, P., Navarro, C., Amiel, J., Boccaccio, I., Lyonnet, S., Stewart, C.L., Munnich, A., Le Merrer, M., and Lévy, N. (2003). Lamin a truncation in Hutchinson-Gilford progeria. Science *300*, 2055.

Duffy, P.H., Feuers, R.J., and Hart, R.W. (1990). Effect of chronic caloric restriction on the circadian regulation of physiological and behavioral variables in old male B6C3F1 mice. Chronobiol. Int. *7*, 291–303.

Dunn, S.E., Kari, F.W., French, J., Leininger, J.R., Travlos, G., Wilson, R., and Barrett, J.C. (1997). Dietary restriction reduces insulin-like growth factor I levels, which modulates apoptosis, cell proliferation, and tumor progression in p53-deficient mice. Cancer Res. *57*, 4667–4672.

Elshorbagy, A.K., Valdivia-Garcia, M., Refsum, H., Smith, A.D., Mattocks, D.A., and Perrone, C.E. (2010). Sulfur amino acids in methionine-restricted rats: hyperhomocysteinemia. Nutrition *26*, 1201–1204.

Enot, D.P., Niso-Santano, M., Durand, S., Chery, A., Pietrocola, F., Vacchelli, E., Madeo, F., Galluzzi, L., and Kroemer, G. (2015). Metabolomic analyses reveal that anti-aging metabolites are depleted by palmitate but increased by oleate in vivo. Cell Cycle *14*, 2399–2407.

Eriksson, M., Brown, W.T., Gordon, L.B., Glynn, M.W., Singer, J., Scott, L., Erdos, M.R., Robbins, C.M., Moses, T.Y., Berglund, P., et al. (2003). Recurrent de novo point mutations in lamin A cause Hutchinson-Gilford progeria syndrome. Nature *423*, 293–298.

Finkel, T. (2015). The metabolic regulation of aging. Nat. Med. *21*, 1416–1423.

Fontana, L., and Partridge, L. (2015). Promoting health and longevity through diet: from model organisms to humans. Cell *161*, 106–118.

Fontana, L., Villareal, D.T., Das, S.K., Smith, S.R., Meydani, S.N., Pittas, A.G., Klein, S., Bhapkar, M., Rochon, J., Ravussin, E., and Holloszy, J.O.; CALERIE Study Group (2016). Effects of 2-year calorie restriction on circulating levels of IGF-1, IGF-binding proteins and cortisol in nonobese men and women: a randomized clinical trial. Aging Cell *15*, 22–27.

Galluzzi, L., Pietrocola, F., Levine, B., and Kroemer, G. (2014). Metabolic control of autophagy. Cell *159*, 1263–1276.

Goldberg, A.A., Richard, V.R., Kyryakov, P., Bourque, S.D., Beach, A., Burstein, M.T., Glebov, A., Koupaki, O., Boukh-Viner, T., Gregg, C., et al. (2010). Chemical genetic screen identifies lithocholic acid as an anti-aging compound that extends yeast chronological life span in a TOR-independent manner, by modulating housekeeping longevity assurance processes. Aging (Albany NY) *2*, 393–414.

Gordon, L.B., Rothman, F.G., López-Otín, C., and Misteli, T. (2014). Progeria: a paradigm for translational medicine. Cell *156*, 400–407.

Heilbronn, L.K., de Jonge, L., Frisard, M.I., DeLany, J.P., Larson-Meyer, D.E., Rood, J., Nguyen, T., Martin, C.K., Volaufova, J., Most, M.M., et al.; Pennington CALERIE Team (2006). Effect of 6-month calorie restriction on biomarkers of longevity, metabolic adaptation, and oxidative stress in overweight individuals: a randomized controlled trial. JAMA *295*, 1539–1548.

Hine, C., Harputlugil, E., Zhang, Y., Ruckenstuhl, C., Lee, B.C., Brace, L., Longchamp, A., Treviño-Villarreal, J.H., Mejia, P., Ozaki, C.K., et al. (2015). Endogenous hydrogen sulfide production is essential for dietary restriction benefits. Cell *160*, 132–144.

Igarashi, M., and Guarente, L. (2016). mTORC1 and SIRT1 cooperate to foster expansion of gut adult stem cells during calorc restriction. Cell *166*, 436–450.

Johnson, S.C., Rabinovitch, P.S., and Kaeberlein, M. (2013). mTOR is a key modulator of ageing and age-related disease. Nature *493*, 338–345.

Lee, S.J., Jung, Y.S., Yoon, M.H., Kang, S.M., Oh, A.Y., Lee, J.H., Jun, S.Y., Woo, T.G., Chun, H.Y., Kim, S.K., et al. (2016). Interruption of progerin-lamin A/C binding ameliorates Hutchinson-Gilford progeria syndrome phenotype. J. Clin. Invest. *126*, 3879–3893.

Leonov, A., Arlia-Ciommo, A., Bourque, S.D., Koupaki, O., Kyryakov, P., Dakik, P., McAuley, M., Medkour, Y., Mohammad, K., Di Maulo, T., and Titorenko, V.I. (2017). Specific changes in mitochondrial lipidome alter mitochondrial proteome and increase the geroprotective efficiency of lithocholic acid in chronologically aging yeast. Oncotarget *8*, 30672–30691.

López-Otín, C., Blasco, M.A., Partridge, L., Serrano, M., and Kroemer, G. (2013). The hallmarks of aging. Cell *153*, 1194–1217.

López-Otín, C., Galluzzi, L., Freije, J.M.P., Madeo, F., and Kroemer, G. (2016). Metabolic control of longevity. Cell *166*, 802–821.

Lorbek, G., Lewinska, M., and Rozman, D. (2012). Cytochrome P450s in the synthesis of cholesterol and bile acids–from mouse models to human diseases. FEBS J. *279*, 1516–1533.

Madeo, F., Pietrocola, F., Eisenberg, T., and Kroemer, G. (2014). Caloric restriction mimetics: towards a molecular definition. Nat. Rev. Drug Discov. *13*, 727–740.

Madeo, F., Zimmermann, A., Maiuri, M.C., and Kroemer, G. (2015). Essential role for autophagy in life span extension. J. Clin. Invest. *125*, 85–93.

Magner, D.B., Wollam, J., Shen, Y., Hoppe, C., Li, D., Latza, C., Rottiers, V., Hutter, H., and Antebi, A. (2013). The NHR-8 nuclear receptor regulates cholesterol and bile acid homeostasis in *C. elegans*. Cell Metab. *18*, 212–224.

Mann, N.J., Li, D., Sinclair, A.J., Dudman, N.P., Guo, X.W., Elsworth, G.R., Wilson, A.K., and Kelly, F.D. (1999). The effect of diet on plasma homocysteine concentrations in healthy male subjects. Eur. J. Clin. Nutr. *53*, 895–899.

Mariño, G., Ugalde, A.P., Salvador-Montoliu, N., Varela, I., Quirós, P.M., Cadiñanos, J., van der Pluijm, I., Freije, J.M., and López-Otín, C. (2008). Premature aging in mice activates a systemic metabolic response involving autophagy induction. Hum. Mol. Genet. *17*, 2196–2211.

Mariño, G., Ugalde, A.P., Fernández, A.F., Osorio, F.G., Fueyo, A., Freije, J.M., and López-Otín, C. (2010). Insulin-like growth factor 1 treatment extends longevity in a mouse model of human premature aging by restoring somatotroph axis function. Proc. Natl. Acad. Sci. USA *107*, 16268–16273.

McCarty, M.F., Barroso-Aranda, J., and Contreras, F. (2009). The low-methionine content of vegan diets may make methionine restriction feasible as a life extension strategy. Med. Hypotheses *72*, 125–128.

Mercken, E.M., Carboneau, B.A., Krzysik-Walker, S.M., and de Cabo, R. (2012). Of mice and men: the benefits of caloric restriction, exercise, and mimetics. Ageing Res. Rev. *11*, 390–398.

Mercken, E.M., Hu, J., Krzysik-Walker, S., Wei, M., Li, Y., McBurney, M.W., de Cabo, R., and Longo, V.D. (2014). SIRT1 but not its increased expression is essential for lifespan extension in caloric-restricted mice. Aging Cell *13*, 193–196.

Miller, R.A., Buehner, G., Chang, Y., Harper, J.M., Sigler, R., and Smith-Wheelock, M. (2005). Methionine-deficient diet extends mouse lifespan, slows immune and lens aging, alters glucose, T4, IGF-I and insulin levels, and increases hepatocyte MIF levels and stress resistance. Aging Cell *4*, 119–125.

Mirzaei, H., Suarez, J.A., and Longo, V.D. (2014). Protein and amino acid restriction, aging and disease: from yeast to humans. Trends Endocrinol. Metab. *25*, 558–566.

Mitchell, S.J., Madrigal-Matute, J., Scheibye-Knudsen, M., Fang, E., Aon, M., González-Reyes, J.A., Cortassa, S., Kaushik, S., Gonzalez-Freire, M., Patel, B., et al. (2016). Effects of sex, strain, and energy intake on hallmarks of aging in mice. Cell Metab. *23*, 1093–1112.

Nakagawa, S., Lagisz, M., Hector, K.L., and Spencer, H.G. (2012). Comparative and meta-analytic insights into life extension via dietary restriction. Aging Cell *11*, 401–409.

Navarro, C.L., Cadiñanos, J., De Sandre-Giovannoli, A., Bernard, R., Courrier, S., Boccaccio, I., Boyer, A., Kleijer, W.J., Wagner, A., Giuliano, F., et al. (2005). Loss of ZMPSTE24 (FACE-1) causes autosomal recessive restrictive dermopathy and accumulation of Lamin A precursors. Hum. Mol. Genet. *14*, 1503–1513.

Niedernhofer, L.J., Garinis, G.A., Raams, A., Lalai, A.S., Robinson, A.R., Appeldoorn, E., Odijk, H., Oostendorp, R., Ahmad, A., van Leeuwen, W., et al. (2006). A new progeroid syndrome reveals that genotoxic stress suppresses the somatotroph axis. Nature *444*, 1038–1043.

Ocampo, A., Reddy, P., Martinez-Redondo, P., Platero-Luengo, A., Hatanaka, F., Hishida, T., Li, M., Lam, D., Kurita, M., Beyret, E., et al. (2016). In vivo amelioration of age-associated hallmarks by partial reprogramming. Cell *167*, 1719–1733.e12.

Orgeron, M.L., Stone, K.P., Wanders, D., Cortez, C.C., Van, N.T., and Gettys, T.W. (2014). The impact of dietary methionine restriction on biomarkers of metabolic health. Prog. Mol. Biol. Transl. Sci. *121*, 351–376.

Osorio, F.G., Navarro, C.L., Cadiñanos, J., López-Mejía, I.C., Quirós, P.M., Bartoli, C., Rivera, J., Tazi, J., Guzmán, G., Varela, I., et al. (2011). Splicing-directed therapy in a new mouse model of human accelerated aging. Sci. Transl. Med. *3*, 106ra107.

Osorio, F.G., Bárcena, C., Soria-Valles, C., Ramsay, A.J., de Carlos, F., Cobo, J., Fueyo, A., Freije, J.M., and López-Otín, C. (2012). Nuclear lamina defects cause ATM-dependent NF-κB activation and link accelerated aging to a systemic inflammatory response. Genes Dev. *26*, 2311–2324.

Parfitt, A.M., Drezner, M.K., Glorieux, F.H., Kanis, J.A., Malluche, H., Meunier, P.J., Ott, S.M., and Recker, R.R. (1987). Bone histomorphometry: standardization of nomenclature, symbols, and units. Report of the ASBMR Histomorphometry Nomenclature Committee. J. Bone Miner. Res. *2*, 595–610.

Pendás, A.M., Zhou, Z., Cadiñanos, J., Freije, J.M., Wang, J., Hultenby, K., Astudillo, A., Wernerson, A., Rodríguez, F., Tryggvason, K., and López-Otín, C. (2002). Defective prelamin A processing and muscular and adipocyte alterations in Zmpste24 metalloproteinase-deficient mice. Nat. Genet. *31*, 94–99.

Pérez-Silva, J.G., Araujo-Voces, M., and Quesada, V. (2018). nVenn: generalized, quasi-proportional Venn and Euler diagrams. Bioinformatics *34*, 2322–2324.

Ritchie, M.E., Phipson, B., Wu, D., Hu, Y., Law, C.W., Shi, W., and Smyth, G.K. (2015). limma powers differential expression analyses for RNA-sequencing and microarray studies. Nucleic Acids Res. *43*, e47.

Scaffidi, P., and Misteli, T. (2006). Lamin A-dependent nuclear defects in human aging. Science *312*, 1059–1063.

Schmidt, J.A., Rinaldi, S., Scalbert, A., Ferrari, P., Achaintre, D., Gunter, M.J., Appleby, P.N., Key, T.J., and Travis, R.C. (2016). Plasma concentrations and intakes of amino acids in male meat-eaters, fish-eaters, vegetarians and vegans: a cross-sectional analysis in the EPIC-Oxford cohort. Eur. J. Clin. Nutr. *70*, 306–312.

Schroeder, E.A., and Brunet, A. (2015). Lipid profiles and signals for long life. Trends Endocrinol. Metab. *26*, 589–592.

Solon-Biet, S.M., Mitchell, S.J., Coogan, S.C., Cogger, V.C., Gokarn, R., McMahon, A.C., Raubenheimer, D., de Cabo, R., Simpson, S.J., and Le Couteur, D.G. (2015). Dietary protein to carbohydrate ratio and caloric restriction: comparing metabolic outcomes in mice. Cell Rep. *11*, 1529–1534.

Stenesen, D., Suh, J.M., Seo, J., Yu, K., Lee, K.S., Kim, J.S., Min, K.J., and Graff, J.M. (2013). Adenosine nucleotide biosynthesis and AMPK regulate adult life span and mediate the longevity benefit of caloric restriction in flies. Cell Metab. *17*, 101–112.

van der Pluijm, I., Garinis, G.A., Brandt, R.M., Gorgels, T.G., Wijnhoven, S.W., Diderich, K.E., de Wit, J., Mitchell, J.R., van Oostrom, C., Beems, R., et al. (2007). Impaired genome maintenance suppresses the growth hormone–insulin-like growth factor 1 axis in mice with Cockayne syndrome. PLoS Biol. *5*, e2.

Varela, I., Cadiñanos, J., Pendás, A.M., Gutiérrez-Fernández, A., Folgueras, A.R., Sánchez, L.M., Zhou, Z., Rodríguez, F.J., Stewart, C.L., Vega, J.A., et al. (2005). Accelerated ageing in mice deficient in Zmpste24 protease is linked to p53 signalling activation. Nature *437*, 564–568.

Vermeij, W.P., Dollé, M.E., Reiling, E., Jaarsma, D., Payan-Gomez, C., Bombardieri, C.R., Wu, H., Roks, A.J., Botter, S.M., van der Eerden, B.C., et al. (2016). Restricted diet delays accelerated ageing and genomic stress in DNA-repair-deficient mice. Nature *537*, 427–431.

Wang, C., Li, Q., Redden, D.T., Weindruch, R., and Allison, D.B. (2004). Statistical methods for testing effects on "maximum lifespan". Mech. Ageing Dev. *125*, 629–632.

Xia, J., Sinelnikov, I.V., Han, B., and Wishart, D.S. (2015). MetaboAnalyst 3.0–making metabolomics more meaningful. Nucleic Acids Res. *43* (*W1*), W251–W257.

Cell Reports, Volume *24*

Supplemental Information

Methionine Restriction Extends Lifespan in Progeroid Mice and Alters Lipid and Bile Acid Metabolism

Clea Bárcena, Pedro M. Quirós, Sylvère Durand, Pablo Mayoral, Francisco Rodríguez, Xurde M. Caravia, Guillermo Mariño, Cecilia Garabaya, María Teresa Fernández-García, Guido Kroemer, José M.P. Freije, and Carlos López-Otín

SUPPLEMENTAL FIGURES

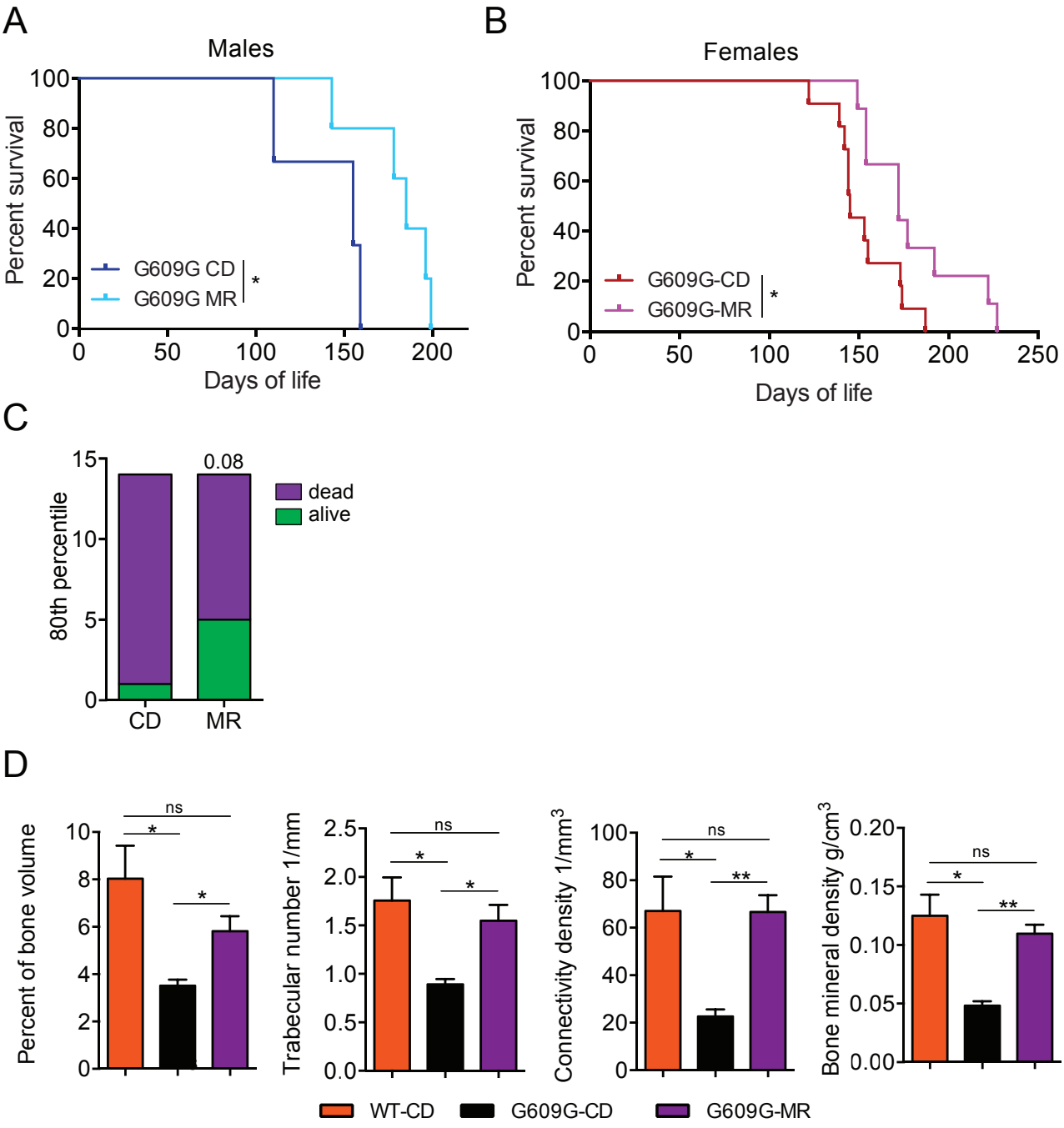

Figure S1. Related to Figure 1. Methionine restriction enhances healthspan and median and maximal lifespan of *Lmna*$^{G609G/G609G}$ mice. (A-B) Survival plot of *Lmna*$^{G609G/G609G}$ mice fed MR diet or control diet in (A) males (n=3-5) and (B) females (n=9-11). Median survival increment is 19.35% for males fed an MR diet ($p<0.05$) and 18.62% for females fed an MR diet ($p<0.05$). Survival curves were analyzed with Log-rank (Mantel-Cox) test (p=0.04 for males and 0.02 for females) and Gehan-Breslow-Wilcoxon test (p=0.07 for males and 0.02 for females). (C) Maximum survival analysis at 80th percentile using Fisher's exact test of *Lmna*$^{G609G/G609G}$ mice fed CD and MR diet. (D) Quantitative analysis of percent of bone volume (bone volume/tissue volume [BV/TV]), trabecular number per mm, connectivity density per mm^3 and bone mineral density (g/cm^3) (n=3). Mean values are represented and error bars indicate SEM. ns: not significant, *$p<0.05$, **$p<0.01$, ***$p<0.001$.

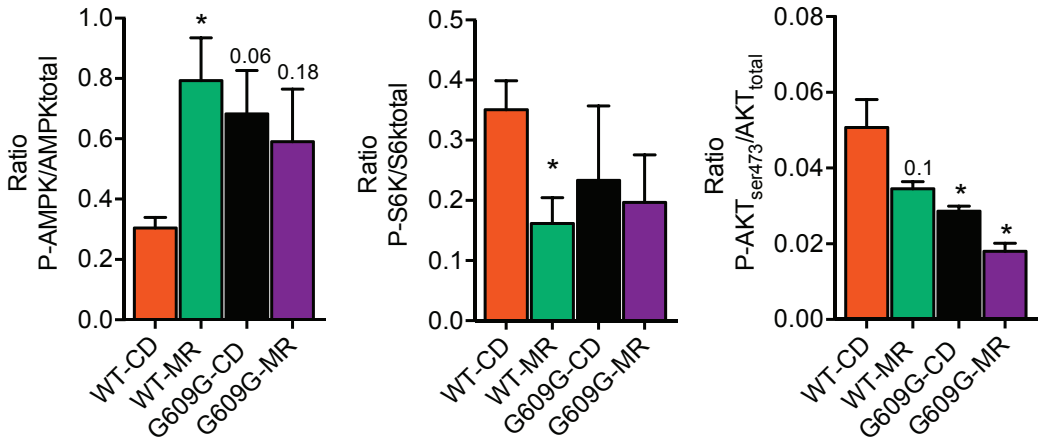

Figure S2. Related to Figure 2. Methionine restriction fails to induce the classical survival response in *Lmna*$^{G609G/G609G}$ mice. Quantification of the ratio of P-AMPK/total-AMPT, P-P70S6K/total-P70S6K and P-AKT(ser473)/total-AKT in liver protein extracts (n=3). *p<0.05.

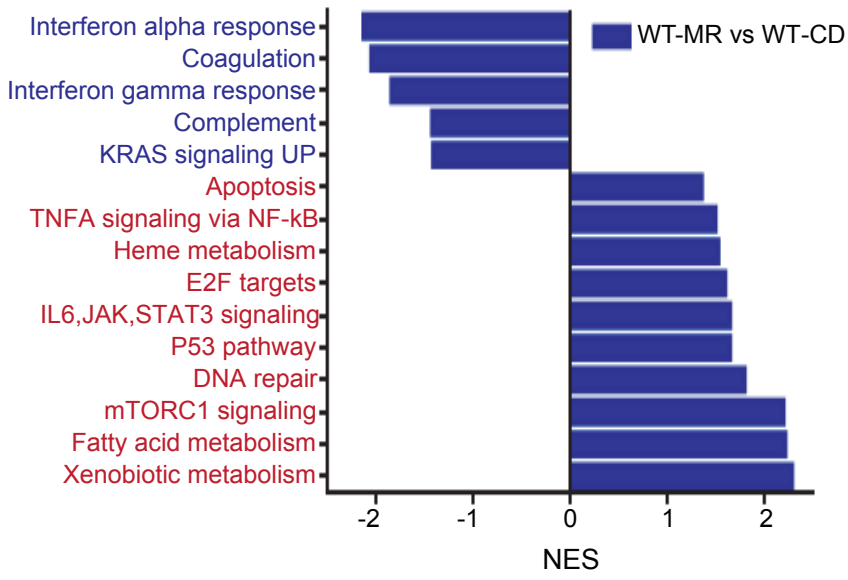

Figure S3. Related to Figure 3. Microarray analysis of liver samples show a shift under methionine restricted diet. GSEA normalized enrichment score (NES) analysis of WT-MR compared to WT-CD. Red color indicates upregulated pathways and blue color downregulated pathways.

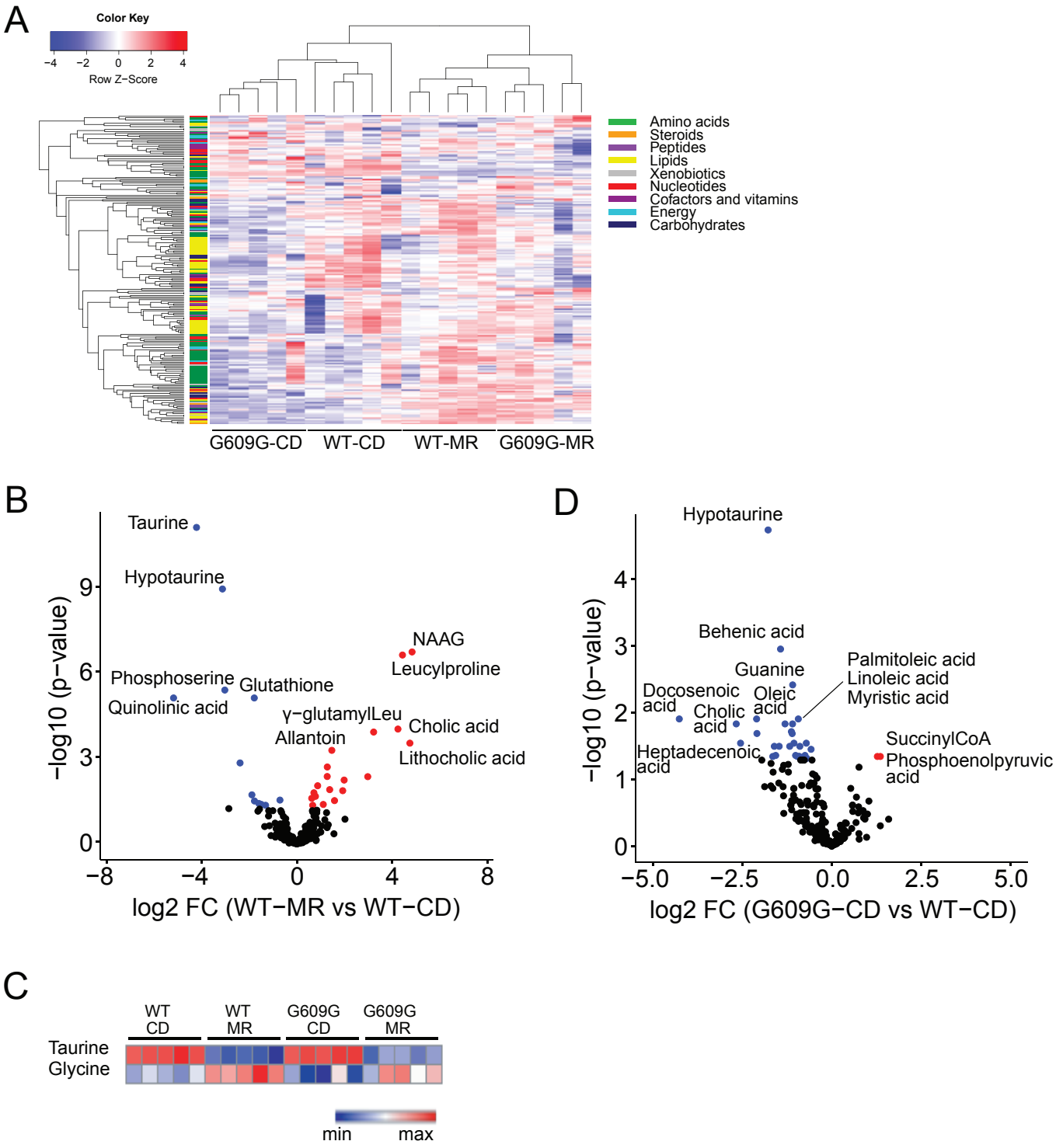

Figure S4. Related to Figure 4. Metabolomic analyses of liver samples show a metabolic shift under methionine restricted diet. (A) Metabolite heatmap based on the differential expression on the detected metabolites. Clusterization proves the similarity between MR samples. (B) Volcano plot showing the most relevant differences of individual metabolites in WT-MR compared to WT-CD mice. Upregulated metabolites are indicated in red and downregulated metabolites in blue. (C) Taurine and glycine relative levels in liver samples represented in a heatmap elaborated with Gene-E software. (D) Volcano plot showing the most relevant differences of individual metabolites in *Lmna*$^{G609G/G609G}$-CD compared to WT-CD mice. Upregulated metabolites are indicated in red and downregulated metabolites in blue.

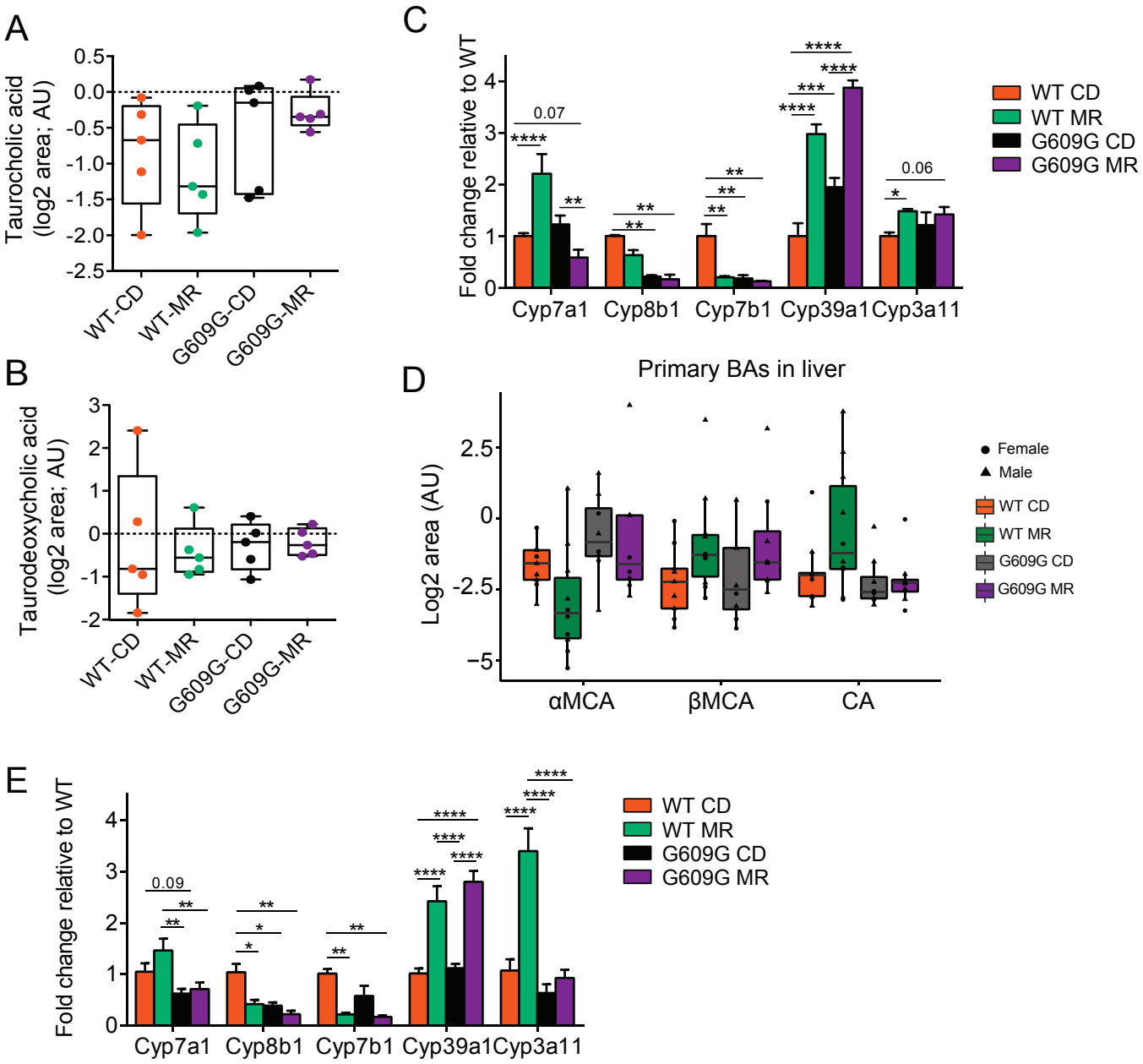

Figure S5. Related to Figure 5. Bile acids profile under methionine restriction in fasting and re-feeding conditions. (A-B) Boxplots showing the levels of (A) taurocholic acid and (B) taurodeoxycholic acid under fasting conditions in liver samples from WT-CD, WT-MR, *Lmna*$^{G609G/G609G}$-CD and *Lmna*$^{G609G/G609G}$-MR (n=5). Levels are indicated as the log2 of the normalized area in arbitrary units (AU). (C) mRNA expression levels of genes involved in bile acid synthesis in liver under fasting conditions. Values are shown as relative to WT-CD mice (n=5). (D) Primary bile acids levels in liver samples from WT-CD, WT-MR, *Lmna*$^{G609G/G609G}$-CD and *Lmna*$^{G609G/G609G}$-MR mice. Levels are indicated as the log2 of the normalized area in AU. Sex is indicated with different symbols (n=8). αMCA: α-muricholic acid; β MCA: β-muricholic acid; CA: cholic acid. (E) mRNA expression levels of genes involved in bile acid synthesis in liver under refeeding conditions. Values are shown as relative to WT-CD mice (n=5). *p<0.05, **p<0.01, ***p<0.001, ****p<0.0001. See also Table S3.

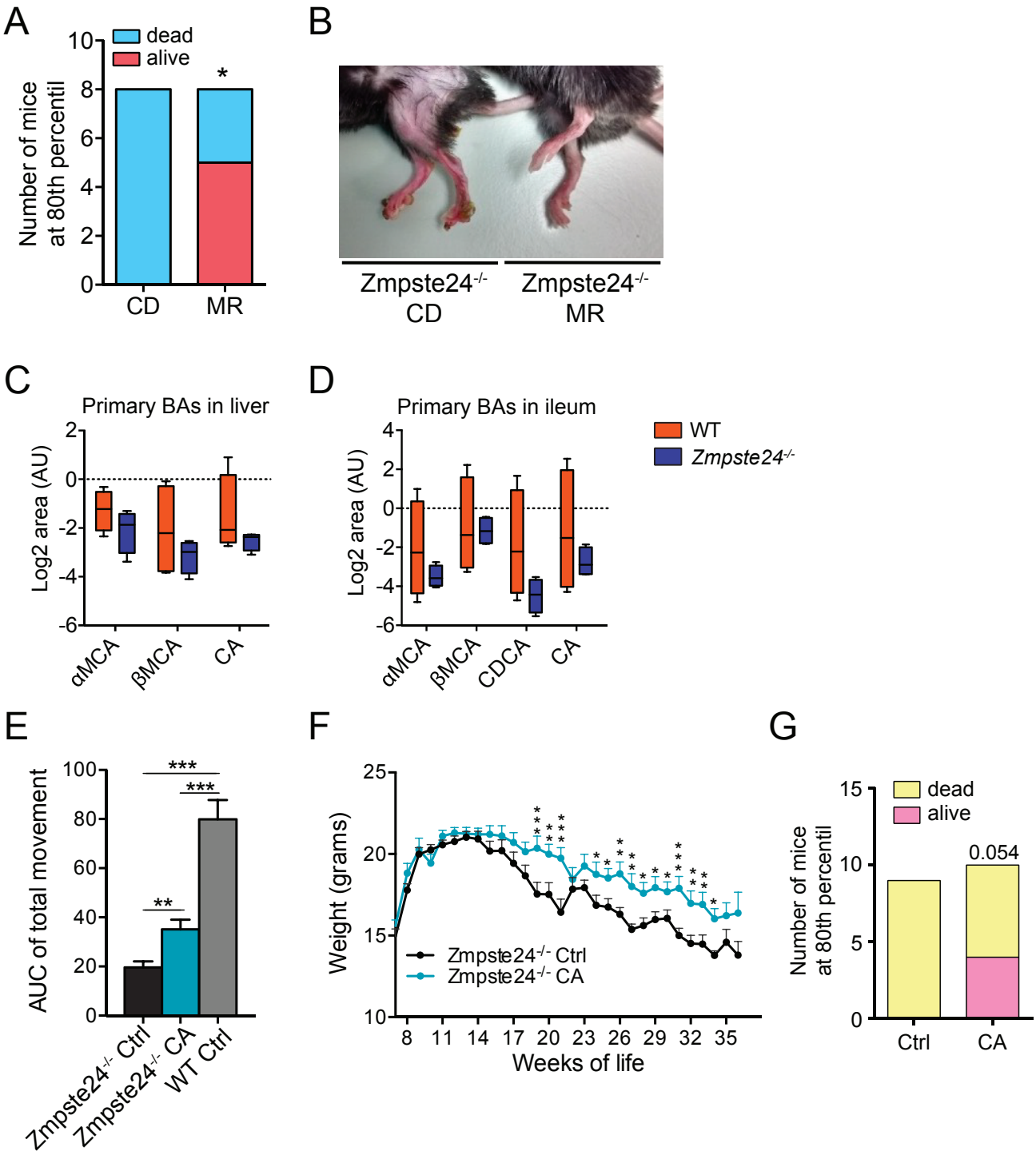

Figure S6. Relative to Figure 6. Methionine restriction and cholic acid supplementation enhance healthspan and lifespan in *Zmpste24*$^{-/-}$ mouse model of HGPS. (A) Maximum survival analysis at 80th percentile using Fisher's exact test of *Zmpste24*$^{-/-}$ mice fed CD and MR diet. (B) *Zmpste24*$^{-/-}$ MR mice (right) have an improved hind limb atrophy than *Zmpste24*$^{-/-}$ CD mice (left). (C-D) Primary bile acids levels in (C) liver and (D) ileum samples from WT and *Zmpste24*$^{-/-}$ mice. Levels are indicated as the log2 of the normalized area in arbitrary units (AU). αMCA: α-muricholic acid; β MCA: β-muricholic acid; CDCA: chenodeoxycholic acid; CA: cholic acid. (E) Area under the curve of the daily movement of WT, *Zmpste24*$^{-/-}$ CA and *Zmpste24*$^{-/-}$ control mice. (F) *Zmpste24*$^{-/-}$ CA show a milder phenotype-associated loss of weight than *Zmpste24*$^{-/-}$ control. (G) Maximum survival analysis at 80th percentile using Fisher's exact test of *Zmpste24*$^{-/-}$ control mice and supplemented with cholic acid. *p<0.05, **p<0.01, ***p<0.001.

Table S3. Related to Figure S5. List of primer sets used for qPCR analyses.

Gene	Forward (5'-3')	Reverse (5'-3')
Cyp3a11	GGTTTATGGAAATTCGACATGGA	GGGTCTGTGACAGCAAGG
Cyp7a1	CTCAGCTCTGGAGGGAATGC	CGCAGAGCCTCCTTGATGA
Cyp7b1	GCCACCTTACTGCTCTCGG	GCCAAGATAAGGAAGCCAACCT
Cyp8b1	CCATAAGACGCCATCCCTCC	AATGTGGGTGAGCCATCAG
Cyp39a1	GGCAACATAAAAGCTCACGGA	CCGTCTCCACCACTTCCAAT
Actb	CTGAGGAGCACCCTGTGCT	GTTGAAGGTCTCAAACATGATCTG
Gapdh	TGTGTCCGTCGTGGATCTGA	CCTGCTTCACCACCTTCTTGAT

SUPPLEMENTAL EXPERIMENTAL PROCEDURES

Analysis of bone structure

All tibia samples were scanned by high-resolution micro-computed tomography (SkyScan 1174, SkyScan, Kontich, Belgium). The small sample-holder device for μCT was used to fit the specimen with the long axis perpendicular to the floor of the specimen holder and the x-ray source. Images were obtained by 50 kV X ray tube voltage and 800 μA. All specimens were scanned using 0.5 mm aluminum filter and at 9.6 μm pixel size resolution. For each specimen, a series of 613 projection images were obtained with a rotation step of 0.3° and frame averaging 2 for a total 180° rotation. The scanning time for each sample was approximately 2 hours using an exposure time of 5500 ms. Flat field correction was performed at the beginning of each scan. The images obtained during scanning were reconstructed using the software NRecon (SkyScan). The correction values of attenuation coefficient, beam hardering, smoothing and ring-artifact reduction were the same in all samples. For morphometric analysis in 2D and 3D it was used the software provided by the manufacturer (CTAn). Region of interest (ROI) was manually delimited in each of the samples. For the analysis of the diaphyseal cortical region 100 slices were chosen. Global grayscale threshold levels for this area were between 88 and 250. For the trabecular region a total of 150 slices were selected and adaptative grayscale threshold levels between 63 and 250 were used. The morphometric parameters examined were bone mineral density (BMD), ratio of bone volume/ tissue volume (BV/TV), and trabecular thickness (Tb.Th), trabecular number (Tb.N) and trabecular separation (Tb.Sp) for the trabecular area and connectivity density among trabeculae. The parameters were measured according to the ASBMR histomorphometry nomenclature (Parfitt et al., 1987).

Western blot analysis

Tissues were collected and immediately frozen in dry ice. About 50 mg of each sample of frozen tissue was homogenized in 300 μL of 100 mM Tris-HCl (pH 7.4), 2% SDS, and 50 mM EDTA with a Polytron homogenizer. After evaluation of the protein concentration with the bicinchoninic acid technique (Pierce BCA protein assay kit), equal amounts of proteins were loaded onto SDS-polyacrylamide gels. After electrophoresis, gels were electrotransferred onto Immobilon-FL polyvinylidene fluoride membranes (Millipore). Membranes were stained with Ponceau to confirm the proper electrotransfer and the equal protein loading. Then, membranes were washed with TBS-T buffer (20 mM Tris at pH 7.4, 150 mM NaCl, 0.05% Tween 20), blocked with 5% nonfat dry milk in TBS-T and incubated overnight at 4 °C with the different primary antibodies. Finally, blots were incubated with 1:10,000 secondary antibody conjugated with horseradish peroxidase (HRP) (Jackson ImmunoResearch Laboratories) in 1.5% nonfat milk in TBS-T for 1 h at room temperature. After washing off the secondary antibody with TBST-T buffer, we developed the immunoreactive bands with Immobilon Western chemiluminescent HRP substrate (Millipore) in a LAS-3000 Imaging System (Fujifilm). For the generation of Figure 2D, three blots with the same samples were ran in parallel. Each total form was analyzed in the same blot as the phosphorylated form after membrane stripping following standard protocols. α -Tubulin was used as sample processing control for protein lysates.

RNA preparation and quantitative PCR

Total RNA from about 30 mg of frozen tissues was extracted using Trizol (Life Technologies) and resuspended in nuclease-free water (Life Technologies). 1–2 μg of total RNA was used for reverse transcription using the QuantiTect Reverse Transcription kit (QIAGEN). 10× diluted cDNA was used for quantitative PCR (qPCR) reactions using Power SYBR Green PCR Master Mix (Life Technologies) in an Applied Biosystems 7300 HT Real-Time PCR System. Results are represented as relative quantification using RQ value ($RQ=2^{-\Delta\Delta Ct}$). Primer sets for qPCR analyses are shown in Table S3.

Serum fatty acid and liver triglycerides

Free fatty acids in serum were assayed using the luminometric Free Fatty Acid Assay Kit from Abnova (KA1667). Triglycerides in liver were assayed using the EnzyChrom Triglyceride Assay Kit from BioAssay Systems (ETGA-200). From liver preparation, 50 mg of tissue was homogenized in 500 μL of 5% Triton X-100 (T9284, Sigma) in phosphate buffered saline. Once homogenized, samples were introduced in a water bath at 80 °C and left inside for 5 min allowing them to reach 100 °C in the water bath. We repeated this two times, allowing the samples to settle at room temperature between cycles. After that, samples were centrifuged at 13,000 rpm for 5 min. The supernatant was recovered and diluted 1:8 in Milli-Q water. 10 μL of this dilution was used for the analysis.

Untargeted metabolomics analysis

30 mg of liver for each condition were first weighted and solubilized into 1.5 mL polypropylene Precellys lysis tubes, with 500 µL of cold (-20 °C) lysate buffer (MeOH/ Water/Chloroform, 9/1/1, -20 °C). They were then homogenized three times for 20 s at 5,000 rpm using Precellys 24 tissue homogenator (Bertin Technologies), followed by a centrifugation (10 min at 15,000 x g, 4 °C). 600 µL of the upper phase of the supernatant were collected. The supernatant was then evaporated in microcentrifuge tubes at 40 °C in a pneumatically-assisted concentrator (Techne DB3). 300 µL of methanol were added to the dried extract and split in two aliquots of 150 µL: the first one was used for the GC-MS analysis and the second one for the LC-MS experiment. Analytical methods and data processing were performed as previously described (Enot et al., 2015). Standard reagents used (acetonitrile, methanol, chloroform, acetic acid and dibutylamine acetate concentrate –DBAA) were all acquired from Sigma Aldrich.

Targeted metabolomics analysis

30 mg of tissues (liver/ileon) for each condition were first weighted and solubilized into 1.5 mL polypropylene microcentrifuge tubes with ceramic beads with 1 mL of cold lysate buffer (MeOH/Water/Chloroform, 9/1/1, -20 °C). They were then homogenized three times for 20 s at 5500 rpm using Precellys 24 tissue homogenator (Bertin Technologies, Montigny-le-Bretonneux, France), followed by a centrifugation (10 min at 15000 g, 4 °C). Targeted metabolomics was perform using Ultra High-Pressure Liquid Chromatography coupled by Mass Spectrometry (UHPLC/MS). Collected supernatant were evaporated in microcentrifuge tubes at 40 °C in a pneumatically-assisted concentrator (Techne DB3, Staffordshire, UK). The LC-MS dried extracts were solubilized with 450 µL of MilliQ water and aliquoted in 4 microcentrifuge tubes (100 µL). For bile acids measurements, one aliquot was transferred to LC vials and injected into LC/MS or kept at -80 °C until injection. Targeted analysis was performed on a RRLC 1260 system (Agilent Technologies, Waldbronn, Germany) coupled to a Triple Quadrupole 6410 (Agilent Technologies) equipped with an electrospray source operating in positive mode. The gas temperature was set to 325 °C with a gas flow of 12 L/min. The capillary voltage was set to 4.5 kV. 10 µL of sample were injected on a Column Poroshell 120 EC-C8 (100 mm x 2.1 mm particle size 2.7 µm) from Agilent technologies, protected by a guard column XDB-C18 (5 mm × 2.1 mm particle size 1.8 µm) and heated at 40 °C by a pelletier oven. The gradient mobile phase consisted of water with 0.2% of formic acid (A) and acetonitrile/isopropanol (1/1; v/v) (B) freshly made. The flow rate was set to 0.3 mL/min, and gradient as follow: initial condition was 70% phase A and 30% phase B, maintained during 1.5 min. Molecules were then eluted using a gradient from 30% to 60% phase B over 9 min. The column was washed using 98% mobile phase B for 2 min and equilibrated using 30% mobile phase B for 2 min. After each injection, the needle was washed twice with isopropanol and thrice with water. The autosampler was kept at 4°C. At the end of the batch of analysis, column was rinsed with 0.3 mL/min of MilliQ water (phase A) and acetonitrile (phase B) as follow: 10% phase B during 20 min, to 90% phase B in 20 min, and maintained during 20 min before shutdown. The collision gas was nitrogen. The scan mode used was the MRM for biological samples. Peak detection and integration of the analytes was performed using the Agilent Mass Hunter quantitative software (B.07.01).

Metabolomics quality control policy

A daily qualification of the instrumentation was set up with automatic tune and calibration processes. These qualifications were completed with double injections of standards mixes, at the beginning and at the end of the run, as for a blank extracted sample to control the background impurities. Mixtures were adapted for each chromatographic method. After the extraction, fractions of each biological sample were pooled to create a Quality Control (QC) sample, use to passivate the column before the analysis with the proper biological matrix and re-injected during the batch to monitor and correct analytical bias occurring during the batch (m/z, retention time and sensitivity drifts) during post acquisition treatment signal.

SUPPLEMENTAL REFERENCES

Enot, D.P., Niso-Santano, M., Durand, S., Chery, A., Pietrocola, F., Vacchelli, E., Madeo, F., Galluzzi, L., and Kroemer, G. (2015). Metabolomic analyses reveal that anti-aging metabolites are depleted by palmitate but increased by oleate in vivo. Cell Cycle *14*, 2399–2407.

Parfitt, A.M., Drezner, M.K., Glorieux, F.H., Kanis, J.A., Malluche, H., Meunier, P.J., Ott, S.M., and Recker, R.R. (1987). Bone histomorphometry: standardization of nomenclature, symbols, and units. Report of the ASBMR Histomorphometry Nomenclature Committee. J Bone Min. Res *2*, 595–610.